bioRxiv preprint doi: https://doi.org/10.1101/2020.10.13.338475; this version posted October 14, 2020. The copyright holder for this preprint (which was not certified by peer review) is the author/funder, who has granted bioRxiv a license to display the preprint in perpetuity. It is made available under aCC-BY 4.0 International license.

Spatial transcriptome sequencing of FFPE tissues at the cellular level

Yang Liu[1,2], Archibald Enninful[1,2], Yanxiang Deng[1,2], and Rong Fan[1,2,3*]

[1] Department of Biomedical Engineering, Yale University, New Haven, CT 06520, USA

[2] Yale Stem Cell Center and Yale Cancer Center, Yale School of Medicine, New Haven, CT 06520, USA

[3]Human and Translational Immunology Program, Yale School of Medicine, New Haven, CT 06520, USA

* to whom all correspondence should be addressed. (R.F., rong.fan@yale.edu)

Abstract Formalin-fixed paraffin-embedded (FFPE) tissues are the most abundant archivable specimens in clinical tissue banks, but unfortunately incompatible with single-cell level transcriptome sequencing due to RNA degradation in storage and RNA damage in extraction. We developed an in-tissue barcoding approach namely DBiT-seq for spatially revolved whole transcriptome sequencing at cellular level, which required no tissue dissociation or RNA exaction, thus potentially more suited for FFPE samples. Herein, we demonstrated spatial transcriptome sequencing of embryonic and adult mouse FFPE tissue sections at cellular level (25μm pixel size) with high coverage (>1,000 genes per pixel). Spatial transcriptome of a E10.5 mouse embryo identified all major anatomical features in the brain and abdominal region. Integration with single-cell RNA-seq data for cell type identification indicated that most tissue pixels were dominated by single-cell transcriptional phenotype. Spatial mapping of adult mouse aorta, atrium, and ventricle tissues identified the spatial distribution of different cell types. Spatial transcriptome sequencing of FFPE samples at cellular level may provide enormous opportunities in a wide range of biomedical research. It may allow us to revisit retrospectively the huge resource of clinical tissue specimens to study human disease mechanisms for the discovery of tissue biomarkers and therapeutic targets

Keywords: spatial transcriptomics, sequencing, FFPE, and cellular resolution,

bioRxiv preprint doi: https://doi.org/10.1101/2020.10.13.338475; this version posted October 14, 2020. The copyright holder for this preprint (which was not certified by peer review) is the author/funder, who has granted bioRxiv a license to display the preprint in perpetuity. It is made available under aCC-BY 4.0 International license.

Clinical tissue samples are often stored as formalin fixed paraffin embedded (FFPE) blocks at room temperature, representing the most abundant resource of archived human specimens. For clinical histopathology and diagnostic purpose, tissue morphology is best preserved in FFPE as compared to other tissue banking methods, especially after prolonged storage[1, 2]. Consequently, a huge volume of clinical FFPE tissue samples are readily available worldwide in hospitals and research institutions, which is a valuable source exploitable for retrospective tissue profiling and human disease research[3]. However, during the sample preparation and storage, nucleic acids including mRNAs in FFPE tissue often lost integrity and became partially degraded or fragmented[4]. In order to perform whole transcriptome analysis of FFPE samples using, for example, RNA sequencing (RNA-seq)[5], a harsh chemical process for tissue decrosslinking, digestion, and RNA extraction and capture is required to retrieve mRNAs, which unfortunately resulted in significant RNA degradation, damage, and loss. The bulk tissue digestion process also resulted in the loss of spatial and cellular information needed to trace the cellular origin of mRNAs[6, 7].

Despite recent breakthroughs in massively parallel single-cell RNA sequencing (scRNA-seq) that have transformed all major fields of biological and biomedical research[8-10], FFPE samples are not yet amenable to single-cell transcriptome sequencing using current techniques. Spatial transcriptomics emerged to address the limitation of scRNA-seq by retaining the spatial information of gene expression in the tissue context essential for a true mechanistic understanding of tissue organization, development, and pathogenesis. All early attempts of spatial transcriptomics were based exclusively on single-molecule fluorescence *in situ* hybridization(smFISH) or image-based in situ sequencing[11-14]. In order to measure the expression of mRNAs at the transcriptome level, it requires repeated hybridization and imaging cycles using high-end advanced fluorescence microscopy, which is technically demanding, very costly, and time consuming. Moreover, most of these methods do not analyze RNAs base-by-base but reply on predesigned probes to detect known sequences only. It is highly desirable to harness the power of Next Generation Sequencing (NGS) to realize high sample throughput, low cost, and genome-wide unbiased profiling of spatial gene expression. A barcoded solid-phase RNA capture approach was developed for coarse resolution (~100μm) spatial transcriptomics using a DNA spot microarray[15], which was recently improved to cellular resolution (~10μm) using self-assembled DNA barcode beads in Slide-seq and HDST[16, 17]. However, these NGS-based spatial transcriptomics methods are also fundamentally limited by the requirement to de-crosslink FFPE tissues and extract RNAs to realize high-coverage transcriptome sequencing at the cellular level.

bioRxiv preprint doi: https://doi.org/10.1101/2020.10.13.338475; this version posted October 14, 2020. The copyright holder for this preprint (which was not certified by peer review) is the author/funder, who has granted bioRxiv a license to display the preprint in perpetuity. It is made available under aCC-BY 4.0 International license.

We have developed high-spatial-resolution spatial omics sequencing vis deterministic barcoding in tissue (DBiT-seq), which was distinct from other NGS-based spatial transcriptome techniques in that it require no de-crosslinking for mRNA release and yielded high-quality transcriptome data from paraformaldehyde(PFA)-fixed tissue sections[18]. How to extend it to high-quality spatial transcriptome sequencing of FFPE tissues at cellular level would be another major leap. Herein, we demonstrated spatial transcriptome mapping of mouse embryo (E10.5) FFPE tissue samples with 25μm spatial pixel size and identified all major tissue types in the brain and abdominal region at the cellular level. Integration with scRNA-seq data allowed for identification of 40+ cell types and revealed that most tissue pixels were dominated by single-cell transcriptomes. Applying it to adult mouse heart (atrium and ventricle) and aorta tissues demonstrated high-coverage (>1000 genes per pixel) spatial transcriptome mapping and the detection of sparse cell types in cardiovascular tissues. This work represents a major leap to unlock the enormous resource of clinical histology specimens for human disease research.

The main workflow for FFPE samples is shown in **Figure 1a**. The banked FFPE tissue block was first microtomed into sections of 5-7 μm in thickness and placed onto a poly-L-lysine-coated glass slide. If the FFPE tissue sections were not to be analyzed right away, they should be stored at -80 °C prior to use in order to reduce RNA oxidative degradation by air exposure. Next, deparaffinization was carried out with standard xylene wash. Afterwards, the tissue section was rehydrated and permeabilized by proteinase K, and then post-fixed again with formalin. The deparaffinized tissue section exhibited a darkened tissue morphology (**Figure 1b**), which was ready for DBiT-seq. Briefly, the 1st PDMS chip with 50 parallel channels was attached onto the tissue slide and a set of DNA barcode A oligos were flowed through the channels along with reverse transcription reagents. In-tissue reverse transcription would produce cDNAs with barcode A incorporated at the 3' end. After removing the 1st PDMS microfluidic chip, a 2nd PDMS chip with another 50 channels perpendicular to the first PDMS chip was placed on top of the tissue. Ligation was then performed in each of the channel by flowing a set of 50 distinct barcode B oligos plus a universal ligation linker, which was complementary to the half-linker sequence in barcode A and B oligos in order to join them together in proximity to form the full barcode A-B. Thus, the ligation would only occur at the intersection of the two flows where both barcode A and barcode B were present. Afterwards, the tissue was imaged and digested to collect cDNA to perform the downstream procedure including template switch, PCR amplification, and tagmentation to prepare the NGS library for paired-end sequencing.

bioRxiv preprint doi: https://doi.org/10.1101/2020.10.13.338475; this version posted October 14, 2020. The copyright holder for this preprint (which was not certified by peer review) is the author/funder, who has granted bioRxiv a license to display the preprint in perpetuity. It is made available under aCC-BY 4.0 International license.

The attachment of PDMS chip to the tissue section was secured with a clamp set, and the clamping force could cause the deformation of tissue section under the microfluidic channel walls. Therefore, after the application of two PDMS microfluidic chips onto the same tissue section in orthogonal directions for cross-flow barcoding, the slight deformation of the tissue surface gave rise to a 2D grid of square features (**Figure 1c**), which allows the precise identification of individual DBiT-seq pixels and the corresponding location and morphology. The quality of cDNAs was evaluated by electrophoretic size distribution and compared between an archived FFPE mouse embryo sample and an FPA-fixed fresh frozen sample (**Figure S1a&b**). We noticed that the FFPE sample cDNA fragment size peaked between 400 and 500 bps, which was shorter than that of the PFA-fixed fresh frozen sample showing the main peaks over 1000 bps. The average size was calculated to be ~600 bps for FFPE and ~1,400 bps for the PFA-fixed fresh frozen sample. This difference was due in part to RNA degradation in FFPE that affected the integrity of RNAs and the accessible RNA segment length after formalin cross-linking of RNAs and proteins. Next, we assessed the quality of spatial transcriptome sequencing data based on total number of genes or unique molecular identifiers (UMIs) per pixel (**Figure 1d**). For FFPE samples, we found the results were variable among different experiments and sample types. For the mouse embryo samples, we obtained on average of 520 UMIs and 355 genes detected per pixel. For the mouse aorta sample, the average number of UMIs or genes per pixel increased to 1830 and 663, respectively. For the adult mouse heart FFPE samples, we detected 3014 UMIs and 1040 genes for atrium and 2140 UMIs and 832 genes for ventricle. In comparison, we revisited the dataset of a PFA-fixed fresh frozen mouse embryo sample analyzed by DBiT-seq, which showed an average of 4688 UMIs and 2100 genes with the same pixel size (25μm). In order to validate the gene expression profile, we compared the pseudo-bulk RNA-seq data constructed from DBiT-seq of mouse embryo FFPE samples with that derived from the PFA-fixed fresh frozen samples, and calculated the Pearson correlation coefficient, yielding an R value of ~0.88 (**Figure S1c**), which demonstrated a good correlation between the two types of experiments despite the difference in tissue origins or cell lineage. We also compared our data to the published fresh frozen coronal hippocampus sample analyzed by Slide-seq and Slide-seqV2, which reported ~280 UMIs and 200 genes detected per spot using unfixed fresh frozen mouse brain tissue samples.

Using an E10.5 mouse embryo FFPE tissue (**Figure 2a**), we conducted DBiT-seq on two adjacent sections from the same embryo, focusing on two different anatomic areas: the brain region (FFPE-1) and the abdominal region (FFPE-2). Integrated clustering analysis of DBiT-seq from both samples using Seurat revealed 10 distinct clusters (**Figure 2b**). Mapping the clusters back to their spatial location identified spatially distinct patterns that could match the anatomical

bioRxiv preprint doi: https://doi.org/10.1101/2020.10.13.338475; this version posted October 14, 2020. The copyright holder for this preprint (which was not certified by peer review) is the author/funder, who has granted bioRxiv a license to display the preprint in perpetuity. It is made available under aCC-BY 4.0 International license.

annotation (**Figure 2c**). Cluster 0 mainly represents the muscle structure in embryo. Cluster 3 covers the central nerve system including neural tube, forebrain and related nervous tissues. Cluster 4 is specific for ganglions, which comprises the brain ganglions and the dorsal root ganglions (**Figure 2c** right). High spatial resolution allows us to observe individual bone pieces in the spine (cluster 6). Liver is largely shown as cluster 7. Heart comprises two layers of pixels with cluster 8 for myocardium and cluster 10 for epicardium. Cluster 9 is largely located inside the neural tube, probably representing a specific subset of neurons. These results demonstrated that high-spatial-resolution DBiT-seq could resolve fine tissue structures close to the cellular level. We further conducted GO analysis (**Figure 2d**) for each cluster, and the GO pathways matched well with the anatomical annotation. The top 10 differentially expressed genes (DEG) were shown in a heatmap (**Figure S2**). We also conducted similar clustering analysis with each tissue sample as a separate dataset and the results revealed the same spatial patterns (**Figure S3**). DEGs for each cluster can be analyzed and compared (**Figure S4**). For example, *Stmn2* and *Mapt2*, which encode microtubule associated proteins and are important for neuron development, were mainly expressed in forebrain and the neural tube. *Fabp7*, a gene encoding the brain fatty acid binding protein, was expressed mainly at the hindbrain. Myosin associated genes, *Myl2*, *Myh7* and *Myl3* were highly enriched in heart. *Slc4a1*, a gene related to blood coagulation, was detected extensively in liver, where most coagulation factors were produced. *Copx*, a heme biosynthetic enzyme encoding gene, was also produced in liver. *Afp*, which encodes alpha-fetoprotein, one of the earliest proteins synthesized by the embryonic liver, was observed exclusively in liver in an organ-specific manner.

We then applied SpatialDE, an unsupervised spatial differential gene expression analysis tool[19], to the mouse embryo FFPE DBiT-seq data. It identified 30 spatial patterns for each of the two FFPE samples (**Figure S5&S6**). GO analysis of the gene sets identified by SpatialDE revealed the biological meaning of each spatial pattern. For FFPE-1, pattern 0 represents neural precursor cell proliferation, whereas pattern 7 corresponds to eye morphogenesis. For FFPE-2, cluster 20 is specific for the heme metabolic process, and cluster 26 is for cardiac muscle contraction in the heart.

To identify the cell types in each pixel, we performed integrated analysis of mouse embryo (E10.5) DBiT-seq data with the same stage mouse embryo scRNA-seq data from literature[20]. We first compared the aggregated “pseudo bulk” data from DBiT-seq and scRNA-seq by unsupervised clustering (**Figure 2e**). DBiT-seq data of FFPE-1 and FFPE-2 lied closely with the E10.5 mouse embryo samples analyzed by scRNA-seq, which validated FFPE DBiT-seq for

bioRxiv preprint doi: https://doi.org/10.1101/2020.10.13.338475; this version posted October 14, 2020. The copyright holder for this preprint (which was not certified by peer review) is the author/funder, who has granted bioRxiv a license to display the preprint in perpetuity. It is made available under aCC-BY 4.0 International license.

capturing the correct embryonic age even with lower coverage or the number of genes detected. We then performed the integrated analysis of these two types of data by combining the transcriptomes of all individual pixels from DBiT-seq with single-cell transcriptomes for clustering analysis in Seurat after normalization with SCTransform [21]. The DBiT-seq pixels conformed to the clusters of scRNA-seq (**Figure 3a**), enabling the transfer of cell type annotations from scRNA-seq data to the spatial pixels and then mapping different cell types back to spatial distribution (**Figure 3d)**. In FFPE-1, cluster 3 mainly consisted of oligodendrocytes. Epithelial cells (cluster 4) and neural epithelial cells (cluster 13) were observed widely in epithelial glands. Interestingly, excitatory neurons (cluster 7) and inhibitory neurons (cluster 17) were both observed in the neural tube but forming a mixed pattern to fulfil their functionally distinct roles in transporting neurotransmitters. This integrative analysis answered an unresolved question in **Figure 2c** with regards to the specific subset of neurons observed in the neural tube by unsupervised clustering. In FFPE-2, several organ-specific cell types were detected. For example, the primitive erythroid cells (cluster 14) crucial for early embryonic erythroid development and the transition from embryo to fetus in developing mammals were strongly enriched in liver[22]. Cardiac muscle cell type was observed mainly in the heart region in agreement with the anatomical annotation. The integrative analysis with published scRNA-seq data could distinguish cell identity more robustly as compared to the standard GO analysis.

We next examined a mouse aorta FFPE tissue section (**Figure 4a**). The aorta tissue block was cross-sectioned, showing a thin wall of the artery along with the surrounding tissue. The heatmaps of gene and UMI counts (**Figure 4b)** showed more than 1000 genes detected in 50% of the tissue pixels. Unsupervised clustering did not show distinct spatial patterns due to the lack of distinct tissue features and the dominance of specific cell types such as smooth muscle cells in this sample (**Figure S7b**). However, when integrated with scRNA-seq reference data from a mouse aorta [23], we could identify six different cell types, including endothelial cells (ECs), arterial fibroblasts (Fibro), macrophages (Macro), monocytes(Mono), neurons and vascular smooth muscle cells (VSMCs). Most cells were ECs, VSMCs and Fibros. We also noticed that there was a layer of enriched smooth muscle cells in the artery wall, which were known to be the major cell type in a large artery [24]. We also performed automatic cell annotation using SingleR to analyze this aorta DBiT-seq data in comparison to the built-in reference dataset provided in the SingleR package from scRNA-seq of mouse tissues (**Figure S7c**). It is worth pointing out that adipocytes that normally exist in the supporting tissue around the artery were readily identified. Meanwhile, the adipocyte-specific genes like *Adipoq* and *Aoc3* were observed to express at high levels in the surround tissue region (**Figure S7d**).

bioRxiv preprint doi: https://doi.org/10.1101/2020.10.13.338475; this version posted October 14, 2020. The copyright holder for this preprint (which was not certified by peer review) is the author/funder, who has granted bioRxiv a license to display the preprint in perpetuity. It is made available under aCC-BY 4.0 International license.

Lastly, we analyzed adult mouse atrium and ventricle FFPE samples using DBiT-seq (**Figure 4f&g**). Although cardiomyocytes only account for 30-40% of the total cell number in a heart, the volume fraction of cardiomyocytes can reach up to 70–80% [25]. Indeed, we observed the expression of muscle-related gene *Myh6* extensively throughput the cardiac tissue (**Figure S8a**), which encodes a protein known as the cardiac alpha (α)-myosin heavy chain. The fact that there is a large volume of cardiomyocytes in this tissue posed a challenge for spatial expression pattern analysis due to the dominance of one specific cell type and the lack of distinct anatomic landmarks. Unsupervised clustering of the DBiT-seq pixels from atrium and ventricle using Seurat could not resolve highly distinct clusters (**Figure S8b&c**). However, when integrated with scRNA-seq reference data from the mouse heart [26], DBiT-seq pixels of atrium and ventricle conformed rather well to single-cell transcriptional clusters generated with the reference data, which showed a total of 15 clusters (**Figure 4h&j**). These clusters were then annotated using the cell types defined by scRNA-seq (**Figure S9**). The result confirmed that cardiomyocytes were still the main cell type in this tissue and observed across multiple spatial clusters (**Figure 5d&f**), for example, cluster 1, cluster 4 and cluster 8 in the atrium. A significant number of endothelial cells were observed, presumably corresponding to microvasculature in myocardium. Other cell types, like fibroblast stromal cells and macrophages were also observed presumably in the interstitial space of cardiomyocyte fibers in the mouse heart.

In summary, we demonstrated spatially resolved transcriptome sequencing of FFPE tissue sections with 25μm pixel size. The data quality in terms of the number of transcripts and genes detected was lower than that from PFA-fixed frozen sections, but still yielded highly meaningful results with ~1000 genes per pixel across whole transcriptome, which is comparable with or even outperformed other high-spatial-resolution (10 or 20μm spot size) spatial transcriptome technologies[16, 17] that currently could only work with fresh frozen samples. Applying our technology to mouse embryo FFPE tissues resulted in the identification of 11 spatial patterns that agreed with anatomical annotations. Integration with published scRNA-seq data further improved cell type identification and revealed that the majority of spatial tissue pixels were dominated by single-cell transcriptomes. We further analyzed adult mouse aorta, atrium and ventricle FFPE tissue samples and revealed a wide range of cell types localized in the interstitial space myocardium or the perivascular supporting tissue. As FFPE samples are widely available and represent the most abundant resource of archivable clinical tissue specimens, we envision that this work will open up new opportunities to revisit the vast amount of archived human tissue specimens to study the mechanisms of pathophysiology and to discover new targets for diagnosis and treatment of human diseases.

bioRxiv preprint doi: https://doi.org/10.1101/2020.10.13.338475; this version posted October 14, 2020. The copyright holder for this preprint (which was not certified by peer review) is the author/funder, who has granted bioRxiv a license to display the preprint in perpetuity. It is made available under aCC-BY 4.0 International license.

Acknowledgements

This research was supported by Packard Fellowship for Science and Engineering (to R.F.), Stand-Up-to-Cancer (SU2C) Convergence 2.0 Award (to R.F.), and Yale Stem Cell Center Chen Innovation Award (to R.F.), National Science Foundation CAREER Award CBET-1351443 (R.F.), National Institutes of Health grants U54 CA209992 (Sub-Project ID: 7297 to R.F.), R01 CA245313 (R.F.), R33 CA196411 (R.F.), R33 CA246711 (R.F), and UG3CA257393, to R.F.). Y.L. was supported by the Society for ImmunoTherapy of Cancer (SITC) Fellowship. The molds for making microfluidic chips were fabricated at the Becton Nanofabrication Center at the Yale University. We used the service provided by the Genomics Core of Yale Cooperative Center of Excellence in Hematology (U54DK106857). Next-generation sequencing was conducted at Yale Stem Cell Center Genomics Core Facility which was supported by the Connecticut Regenerative Medicine Research Fund and the Li Ka Shing Foundation. It was also conducted using the sequencing facility at the Yale Center for Genomic Analysis (YCGA).

Author contributions

Conceptualization: Y.L, R.F.; Methodology, Y.L., A.E., and Y.D.; Experimental investigation, Y.L., A.E., and Y.D.; Data Analysis, Y.L., A.E., and Y.D. and R.F.; Writing – Original Draft, Y.L. and R.F.; Writing – Review and Editing, Y.L., A.E., Y.D. and R.F..

Conflict of interests

R.F. is scientific founder and advisor of IsoPlexis, Singleron Biotechnologies, and AtlasXomics. The interests of R.F. were reviewed and managed by Yale University Provost's Office in accordance with the University's conflict of interest policies.

Supplemental information

Supplementary Information can be found online at [to be inserted, SI is also provided as part of the manuscript submission].

bioRxiv preprint doi: https://doi.org/10.1101/2020.10.13.338475; this version posted October 14, 2020. The copyright holder for this preprint (which was not certified by peer review) is the author/funder, who has granted bioRxiv a license to display the preprint in perpetuity. It is made available under aCC-BY 4.0 International license.

Materials and Methods

Fabrication of microfluidic device

Soft lithography was used to produce the PDMS (polydimethylsiloxane) microfluidic device. The chrome mask was printed by the company Front Range Photomasks (Lake Havasu City, AZ) with high resolution (2 μm). Upon receiving, chrome mask was cleaned using acetone before use to remove any dirt or dust. The negative photoresist SU-8 (SU-8 2025) based mold was fabricated according to manufacturer's (MicroChem) recommendations using a precleaned silicon wafer substrate. The final SU-8 layer of the mold had a thickness of ~25 μm and a channel width of 25 μm. The fabrication of PDMS microfluidic chips were through a replication molding process. The GE RTV PDMS part A and part B were mixed thoroughly with a 10:1 ratio and poured onto the mold. After degassing for 30min, the PDMS was cured in a 75 °C oven for 2 hours. The cured PDMS slab was then cut and punched with inlet and outlet holes using a 2 mm diameter puncher. The acrylic clamps (rectangle, 22 mm x 40 mm) to strength the attachment of PDMS to glass slide were fabricated using a laser cutter.

Tissue Handling

FFPE samples of adult mouse and mouse embryo were obtained from Zyagen (San Diego, CA). According to Zyagen protocol, the mice used in this project were purchased from Charles River Laboratories. Adult mice were sacrificed upon arrival, and the aorta, atrium and ventricle were collected. The embryo (E10.5) were collected the day the pregnant mouse was received. The FFPE tissues were processed following standard protocols, which includes fixation (10% formalin), dehydration (ethanol series: 70%-100%), clearing (100% xylene), paraffin infiltration and embedding. FFPE sample was sectioned with a thickness of 5-7 μm and placed onto a poly-L-lysine coated glass slide. After receiving the sectioned FFPE slides, the tissue sections were stored at -80 °C in a sealed bag until use.

Deparaffinization of tissue section

Prior to deparaffinization, adult mouse or mouse embryo FFPE tissue slides were first baked at 60°C for 1 hour to ensure that the tissue sections were properly attached to glass slide. Deparaffinization was performed by two times washing with Xylene (100%) for 5 minutes each. To remove the remaining xylene, the section was washed 5 minutes with 100% ethanol. Tissue was then rehydrated by immersing in 90%, 70% and 50% ethanol for 5 minutes each, and finally placed in PBS with 0.1% Tween-20. The tissue was permeabilized for 5 minutes with Proteinase K 7.5μg/ml in PBST and fixed in 4% formaldehyde with 0.2% Glutaraldehyde for 20 minutes.

bioRxiv preprint doi: https://doi.org/10.1101/2020.10.13.338475; this version posted October 14, 2020. The copyright holder for this preprint (which was not certified by peer review) is the author/funder, who has granted bioRxiv a license to display the preprint in perpetuity. It is made available under aCC-BY 4.0 International license.

DNA oligo design

Two sets of DNA barcodes (A1:A50 and B1:B50) were used in this study. Barcode A1:A50 had three different functional regions: a 16-mer poly-T region, an 8-mer spatial barcode region (mark Y-axis location) and a 15-mer ligation linker region (See example Barcode A below). Barcode A1:A50 served as the RT primer and was loaded into each of the 50 channels of the 1st PDMS along with reverse transcription mix. The resulting cDNA products were then ligated to the barcode B1:B50 during the ligation process. There were four different functional parts in barcode B: a 15-mer ligation linker, an 8-mer spatial barcode region(mark X-axis location), a 10-mer unique molecular identifier (UMI), and a PCR handle functionalized with biotin, which is used for purification purpose. Before loading into the 2nd PDMS, barcode B was first annealed to a complementary ligation linker strand and then mixed with DNA ligase reaction mix. The ligation product baring the x and y location information was then extracted and processed with downstream steps. There were theoretically 2,500 pixels in a tissue region of 2.5 mm x 2.5 mm square.

DNA barcode Examples

Barcode A1:

/5Phos/AGGCCAGAGCATTCGAACGTGATTTTTTTTTTTTTTTTVN

Barcode B1:

/5Biosg/CAAGCGTTGGCTTCTCGCATCTNNNNNNNNNNAACAACCAATCCACGTGCTTGAG

DNA Oligos and barcodes used in this paper were listed in Table S1 and all other reagents were listed as Table S2 and S3.

In tissue reverse transcription with Barcode A

The deparaffinized tissue section was blocked by 1% BSA solution in PBS plus RNase inhibitor (0.05U/μL, Enzymatics) for 30 minutes at room temperature. After 3-times washing with 1X PBS and 1-time wash with water, the 1st PDMS slab with 50 channels was placed on the glass slide, covering the interested tissue region. The brightfield image (10x, Thermo Fisher EVOS fl microscope) was recorded and used later for the identification of pixel locations. Afterwards, an acrylic clamp with screws was clamped against the center tissue region of interest.

The Reverse Transcription solution (225 μL) was first prepared by mixing:

50 μL of RT buffer (5X, Maxima H Minus kit),

32.8 μL of RNase free water,

1.6 μL of RNase Inhibitor (Enzymatics),

bioRxiv preprint doi: https://doi.org/10.1101/2020.10.13.338475; this version posted October 14, 2020. The copyright holder for this preprint (which was not certified by peer review) is the author/funder, who has granted bioRxiv a license to display the preprint in perpetuity. It is made available under aCC-BY 4.0 International license.

3.1 μL of SuperaseIn RNase Inhibitor (Ambion),

12.5 μL of dNTPs (10 mM, Thermo Fisher),

25 μL of Reverse Transcriptase (Thermo Fisher),

100 μL of 0.5X PBS with Inhibitor (0.05U/μL, Enzymatics).

After vortex mixing, the RT solution was aliquoted into 50 different tubes, with each tube a 4.5 μL solution. Then, into each tube, a 0.5 μL of barcodes A (A1-A50) (25 μM) was added and mixed thoroughly. The 50 tubes of 5 μL of RT reaction solution were loaded into the 50 inlets (each can hold >10 μL solution) on the PDMS. In order to fill up the channel and remove air bubbles, the solution was pulled through each of the 50 channels with vacuum continuously for 3 minutes. The chip was then put into a wet box and incubated at room temperature for 30 minutes and then at 42 °C for another 1.5 hours. After RT, the channels were cleaned up by 1X NEB buffer 3.1(New England Biolabs) with 1% RNase inhibitor (Enzymatics) continuously for 10 minutes. Finally, the clamp and PDMS were removed from the tissue slide. The slide was quickly dipped in water and dried with air.

In tissue ligation with Barcode B

The 2nd PDMS slab with channels perpendicular to the 1st PDMS was attached to the dried slide with care. A brightfield image was taken (10x, Thermo Fisher EVOS fl microscope) and the same clamp was used here to press the PDMS against the tissue. We then prepared 115.8 μL ligation mix by adding the following reagents into a 1.5 mL Eppendorf tube.

69.5 μL of RNase free water,

27 μL of T4 DNA ligase buffer (10X, New England Biolabs),

11 μL T4 DNA ligase (400 U/μL, New England Biolabs),

2.2 μL RNase inhibitor (40 U/μL, Enzymatics),

0.7 μL SuperaseIn RNase Inhibitor (20 U/μL, Ambion),

5.4 μL of Triton X-100 (5%).

DNA barcode B was first annealed with ligation linker by adding 25 μL of Barcode B (100 μM), 25 μL of ligation linker (100 μM) and 50 μL of annealing buffer (10 mM Tris, pH 7.5 - 8.0, 50 mM NaCl,1 mM EDTA). 5 μL ligation reaction solution (totally 50 tubes) was prepared by adding 2 μL of ligation mix, 2 μL of NEB buffer 3.1(1X, New England Biolabs) and 1 μL of each DNA barcode B and ligation linker mix (B1-B50, 25 μM) and then loaded into each of the 50 channels with vacuum. The chip was kept in a wet box and incubated at 37 °C for 30 minutes. After washing by flowing 1X PBS with 0.1% Triton X-100 and 0.25% SUPERase In RNase Inhibitor for 10 minutes, the clamp and PDMS were removed, and the dried slide was ready for tissue digestion.

bioRxiv preprint doi: https://doi.org/10.1101/2020.10.13.338475; this version posted October 14, 2020. The copyright holder for this preprint (which was not certified by peer review) is the author/funder, who has granted bioRxiv a license to display the preprint in perpetuity. It is made available under aCC-BY 4.0 International license.

Tissue digestion

After removing the 2nd PDMS, the tissue section was dipped in water and dried with air before taking the final brightfield image. Afterwards, we prepared proteinase K lysis solution, which contains 2 mg/mL proteinase K (Thermo Fisher), 10 mM Tris (pH = 8.0), 200 mM NaCl, 50 mM EDTA and 2% SDS. We then covered the tissue region of interest with a square well PDMS gasket and then loaded around ~25 μL of lysis solution into it. The lysis was performed at 55 °C for 2 hours in a wet box. The tissue lysate was collected into a 1.5 mL Eppendorf tube and purified using streptavidin beads (Dynabeads MyOne Streptavidin C1 beads, Thermo Fisher) or stored at -80 °C until use.

cDNA extraction

Before extraction, RNase free water was first added into the lysate to bring the total volume up to 100 μL. 5 μL of PMSF (100 μM, Sigma) was added to the lysate and incubated for 10 minutes at room temperature to inhibit the activity of Proteinase K. Meanwhile, the magnetic beads were cleaned three times with 1X B&W buffer with 0.05% Tween-20 and dispersed into 100 μL of 2X B&W buffer (with 2 μL of SUPERase In Rnase Inhibitor). After adding 100 μL of the cleaned streptavidin beads suspension to the lysate, the mixture was incubated for 60 minutes at room temperature with gentle shaking. Afterwards, the beads were washed twice with 1X B&W buffer and 1X Tris buffer (with 0.1% Tween-20) once.

Template switch

After cleaning, the beads were resuspended into 132 μL of the template switch reaction mix, which consists of:

44 μL 5X Maxima RT buffer (Thermo Fisher),
44 μL of 20% Ficoll PM-400 solution (Sigma),
22 μL of 10 mM dNTPs each (Thermo Fisher),
5.5 μL of RNase Inhibitor (Enzymatics),
11 μL of Maxima H Minus Reverse Transcriptase (Thermo Fisher),
5.5 μL of a template switch primer (100 μM).

Template switch was performed first at room temperature for 30 minutes and then at 42 °C for 90 minutes. After reaction, the beads were pulled down using the magnetic stand and rinsed once with 500 μL 10 mM Tris plus 0.1% Tween-20, and then cleaned with 500 μL RNase free water.

bioRxiv preprint doi: https://doi.org/10.1101/2020.10.13.338475; this version posted October 14, 2020. The copyright holder for this preprint (which was not certified by peer review) is the author/funder, who has granted bioRxiv a license to display the preprint in perpetuity. It is made available under aCC-BY 4.0 International license.

PCR amplification

There are two separate PCR processes. In the first PCR, the cleaned beads with template switched cDNAs were first resuspended into the PCR mix, which contains 110 μL Kapa HiFi HotStart Master Mix (Kapa Biosystems), 8.8 μL of 10 μM stocks of primers 1 and 2, and 92.4 μL of water. The mix were aliquoted into 4 different PCR tubes, with each ~50 μL of solution. Then, PCR reaction was performed with the following steps: incubate at 95°C for 3 mins, then cycle five times at

98°C for 20 seconds,

65°C for 45 seconds,

72°C for 3 minutes.

After reaction, the beads were removed, and the supernatant was collected and pipetted into 4 new PCR tubes. A second PCR was performed by first incubating at 95°C for 3 minutes, then cycled 20 times at

98°C for 20 seconds,

65°C for 20 seconds,

72°C for 3 minutes.

The PCR product was kept in 4°C until next step.

Sequencing library preparation

To remove remaining PCR primers, the PCR product was purified using the Ampure XP beads (Beckman Coulter) at 0.6x ratio following standard protocol. The purified cDNA was then quantified by an Agilent Bioanalyzer High Sensitivity Chip. A Nextera XT Library Prep Kit (Illumina, FC-131-1024) was used to prepare the sequencing library. 1 ng of the cDNA was used as the starting material, and the library preparation is following manufacture protocols. The library was then analyzed by bioanalyzer again and sequenced using a HiSeq 4000 sequencer with pair-end 100x100 mode.

DBiT-seq data pre-processing

Read 1 of the raw sequencing data contains the transcriptome information, while Read 2 holds the UMI, Barcode A and Barcode B. Following ST pipeline v1.7.2[27], Read 1 was trimmed, filtered, STAR mapped (STAR version 2.6.0a) against the mouse genome(GRCh38) and annotated using Gencode release M11. Most of the default parameters were used when running ST pipeline, except that the "--min-length-qual-trimming" was set to 10. The final expression matrix has the

bioRxiv preprint doi: https://doi.org/10.1101/2020.10.13.338475; this version posted October 14, 2020. The copyright holder for this preprint (which was not certified by peer review) is the author/funder, who has granted bioRxiv a license to display the preprint in perpetuity. It is made available under aCC-BY 4.0 International license.

location info as rows and gene expression levels as columns. R package "ggolot2" was used to plot the spatial heatmaps for pan-mRNA or individual genes.

UMI and Gene Counts comparison with other techniques

To compare with other NGs based spatial RNA-seq technique (Fresh Frozen tissue sections), we downloaded published data:

10X Visium: 151673_filtered_feature_bc_matrix.h5 (human cortex)

Slide-seq: Puck_180413_7(coronal hippocampus)

Slide-seqV2: Hippocampus_MappedDGEForR.csv (coronal hippocampus)

DBiT-seq: Mouse embryo Brain E11 25μm resolution

The total UMI and Gene counts were calculated for each of the spots(pixels) and then the violin plots for each technique were plotted side-by-side.

Pseudo bulk comparison with reference

The pseudo bulk data for FFPE samples were obtained by summing counts for each gene in each sample and divided by the sum of total UMI counts, and further multiplied by 1 million. Similarly, the pseudo bulk data was calculated using the E9.5-E13.5 embryo scRNA-seq data from Reference paper [20].

Clustering with Seurat

We used Seurat V3.2[28, 29] to analyze the spatial transcriptome data of all the FFPE samples. Data integration and normalization were performed with the SCTransform workflow. The top 3,000 variable features were selected when doing data integration. For PCA analysis and UMAP visualization, the dimensions were set to 10, and the clustering resolution was set to 0.8. Differentially expressed genes for each cluster was obtained by comparison of cells in individual clusters against all remaining cells.

SpatialDE analysis

To study spatial patterns of gene expression, SpatialDE, an unsupervised automatic expression analysis tool was conducted for both adult heart and mouse embryo samples. Following standard workflow, SpatialDE identified >15 distinct spatial patterns in the mouse embryo sample. The results agree with Seurat pixel-based clustering results.

Cell type annotation

bioRxiv preprint doi: https://doi.org/10.1101/2020.10.13.338475; this version posted October 14, 2020. The copyright holder for this preprint (which was not certified by peer review) is the author/funder, who has granted bioRxiv a license to display the preprint in perpetuity. It is made available under aCC-BY 4.0 International license.

Cell type annotation was achieved by integration analysis (Seurat V3.2, SCTransform) combining the spatial transcriptome data of FFPE samples and the corresponding published scRNA-seq reference. After clustering, the spatial pixel data conformed well with the scRNA-seq data, and thus the cell types were assigned based on the scRNA-seq cell type annotation for each cluster (if two cell types presented in one cluster, the major cell types were assigned). SingleR is also used for aorta sample annotation with the built-in reference "MouseRNAseqData" [30].

GO analysis

GO analysis was completed using the "GO Enrichment Analysis" module at http://geneontology.org/ with default settings. The biological process was ranked by the gene ratio and the top 3-5 biological process were plotted using the "dotplot" function in ggplot2.

Data sharing and codes

Data is available at : https://www.ncbi.nlm.nih.gov/geo/query/acc.cgi?acc=GSE156862. Codes for data analysis are available (https://github.com/rongfan8/DBiT-seq_FFPE).

Methods section reference

Aran, D., Looney, A.P., Liu, L., Wu, E., Fong, V., Hsu, A., Chak, S., Naikawadi, R.P., Wolters, P.J., Abate, A.R., *et al.* (2019). Reference-based analysis of lung single-cell sequencing reveals a transitional profibrotic macrophage. Nat Immunol *20*, 163-172.

Butler, A., Hoffman, P., Smibert, P., Papalexi, E., and Satija, R. (2018). Integrating single-cell transcriptomic data across different conditions, technologies, and species. Nat Biotechnol *36*, 411-420.

Cao, J., Spielmann, M., Qiu, X., Huang, X., Ibrahim, D.M., Hill, A.J., Zhang, F., Mundlos, S., Christiansen, L., Steemers, F.J., *et al.* (2019). The single-cell transcriptional landscape of mammalian organogenesis. Nature *566*, 496-502.

Navarro, J.F., Sjöstrand, J., Salmén, F., Lundeberg, J., and Ståhl, P.L. (2017). ST Pipeline: an automated pipeline for spatial mapping of unique transcripts. Bioinformatics *33*, 2591-2593.

Stuart, T., Butler, A., Hoffman, P., Hafemeister, C., Papalexi, E., Mauck III, W.M., Hao, Y., Stoeckius, M., Smibert, P., and Satija, R. (2019). Comprehensive integration of single-cell data. Cell *177*, 1888-1902. e1821.

bioRxiv preprint doi: https://doi.org/10.1101/2020.10.13.338475; this version posted October 14, 2020. The copyright holder for this preprint (which was not certified by peer review) is the author/funder, who has granted bioRxiv a license to display the preprint in perpetuity. It is made available under aCC-BY 4.0 International license.

Figures and Figure Captions

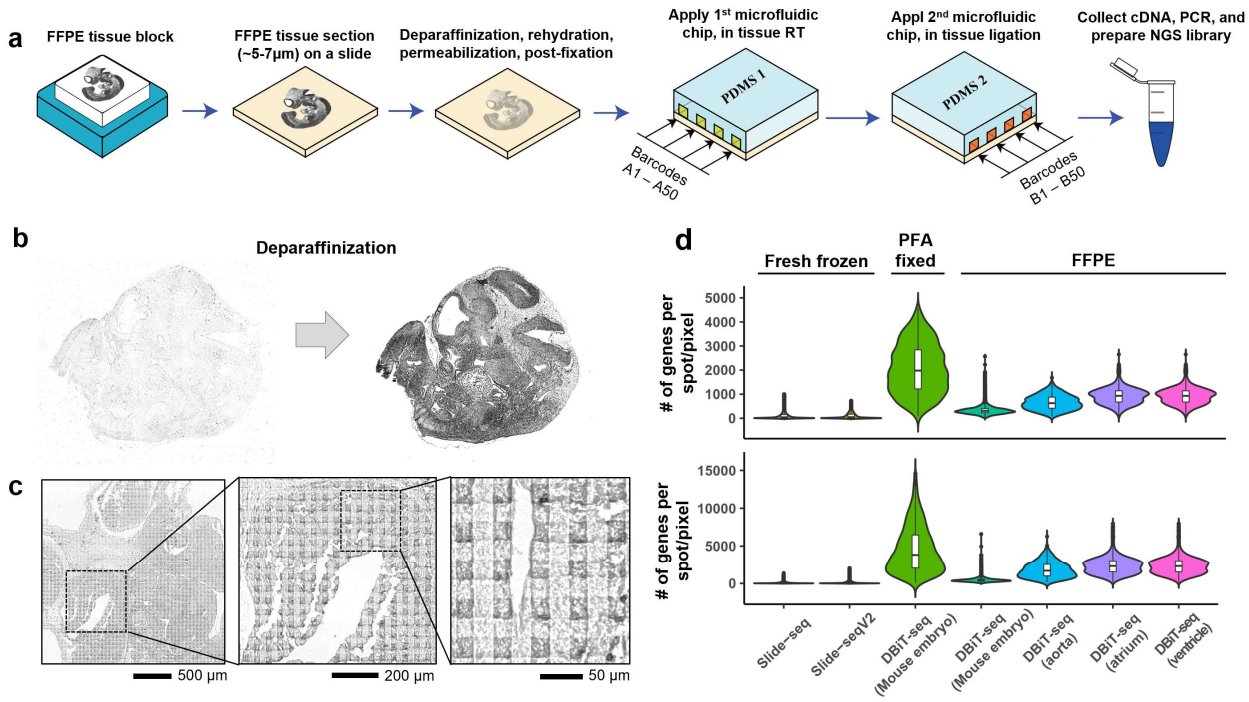

Figure 1. Workflow of DBiT-seq on FFPE samples. (a) Scheme of DBiT-seq on FFPE samples. FFPE tissue blocks stored at room temperature were sectioned into thickness of ~5-7 μm and placed onto a poly-L-lysine coated glass slide. Deparaffinization, rehydration, permeabilization and post-fixation were performed sequentially before placing the 1st PDMS chip on the tissue section. Barcodes A1-A50 were flowed into the microchannels and the reverse transcription was carried out inside each channel. After washing, the 1st PDMS was removed and a 2nd PDMS chip with channels of perpendicular direction was attached on the tissue slide. Ligation reaction mix along with DNA Barcodes B1-B50 were pulled through each of the 50 channels by vacuum and incubated for 30 minutes to perform in situ ligation. Afterwards, the tissue section was digested with Proteinase K to collect cDNA for the downstream processes including template switch, PCR amplification, and tagmentation for NGS library preparation. (b) Deparaffinization of a E10 mouse embryo tissue. It maintained the original morphology with higher contrast after deparaffinization and the fine tissue features were readily discernable. (c) Deformation of tissue section after two sequential microfluidic flows of DBiT-seq. (d) Comparison of gene and UMI counts of our DBiT-seq data from FFPE samples with those obtained from other methods including Slide-seq, Slide-seqV2 and previous DBiT-seq data from PFA-fixed mouse embryo samples.

bioRxiv preprint doi: https://doi.org/10.1101/2020.10.13.338475; this version posted October 14, 2020. The copyright holder for this preprint (which was not certified by peer review) is the author/funder, who has granted bioRxiv a license to display the preprint in perpetuity. It is made available under aCC-BY 4.0 International license.

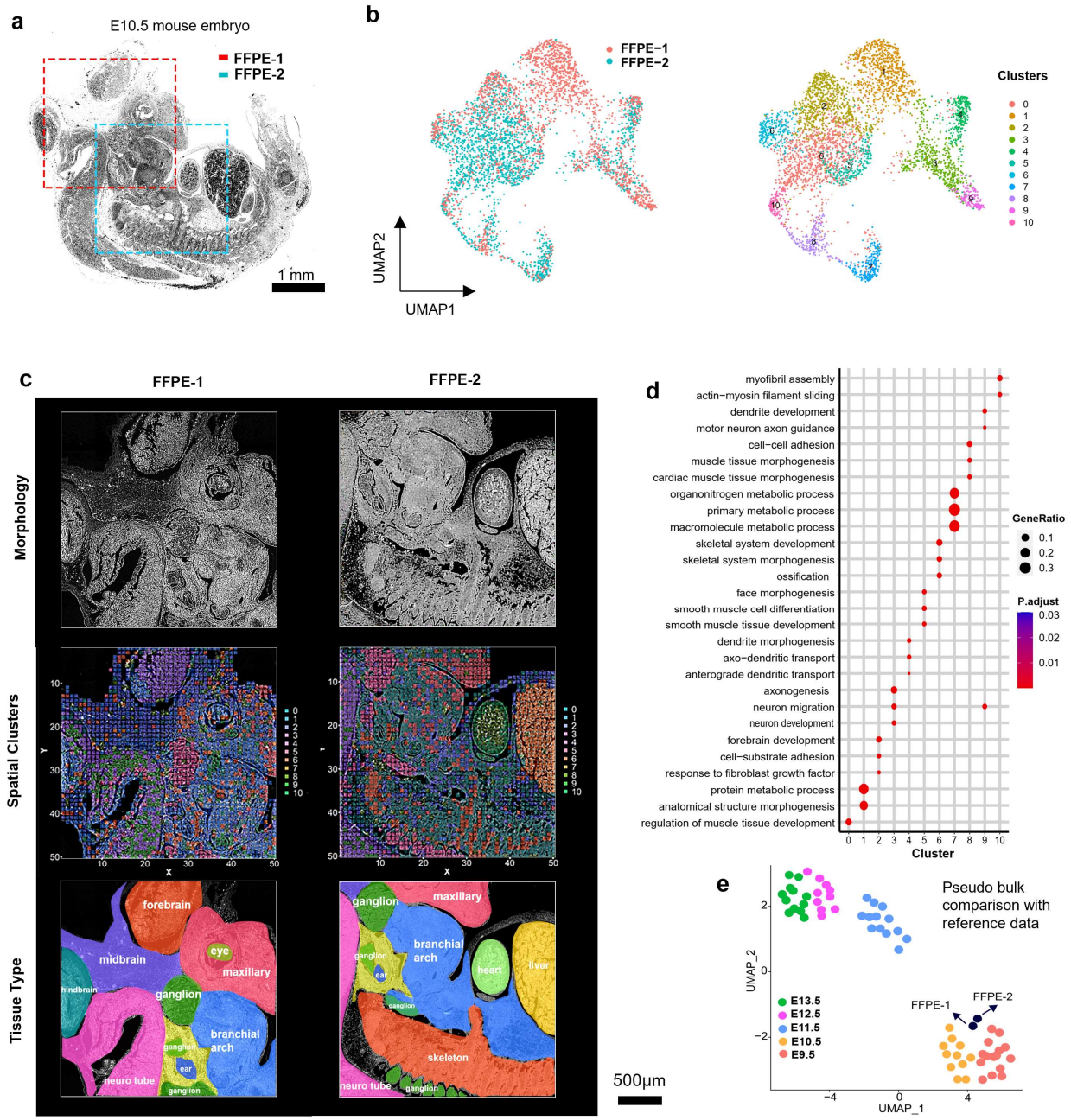

Figure 2. Spatial transcriptome analysis of FFPE tissue sections from an E10.5 mouse embryo. (a) Two tissue regions of FFPE mouse embryo were analyzed using DBiT-seq. One (FFPE-1) covered the brain region of the mouse embryo and the other (FFPE-2) covered the mid-body abdominal region. Two separate tissue sections were used in this study. (b) UMAP visualization of combined pixels from FFPE-1 and FFPE-2 using Seurat package. Left: UMAP labelled by sample names; right: UMAP labelled by cluster numbers. Totally 10 clusters were identified. (c) Tissue morphology, anatomical annotation, and spatial mapping of the 11 clusters in (b). (d) GO enrichment analysis of all clusters (0-10). (e) Comparison of "pseudo bulk" data

bioRxiv preprint doi: https://doi.org/10.1101/2020.10.13.338475; this version posted October 14, 2020. The copyright holder for this preprint (which was not certified by peer review) is the author/funder, who has granted bioRxiv a license to display the preprint in perpetuity. It is made available under aCC-BY 4.0 International license.

between DBiT-seq and scRNA-seq reference data. The aggregated transcriptome profiles of DBiT-seq from two FFPE samples conform well into scRNA-seq reference data from mouse embryos ranging from E9.5-E13.5(Cao et al., 2019).

bioRxiv preprint doi: https://doi.org/10.1101/2020.10.13.338475; this version posted October 14, 2020. The copyright holder for this preprint (which was not certified by peer review) is the author/funder, who has granted bioRxiv a license to display the preprint in perpetuity. It is made available under aCC-BY 4.0 International license.

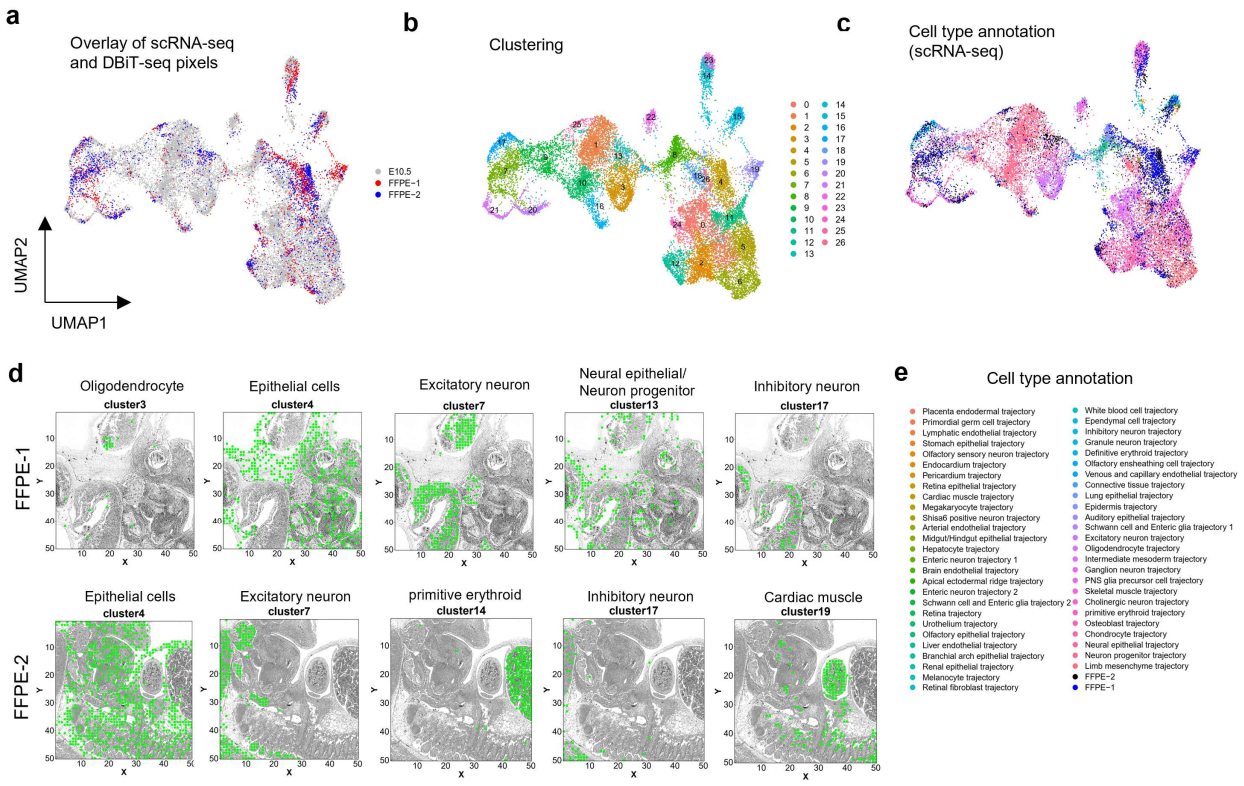

Figure 3. Integrative analysis of scRNA-seq and DBiT-seq (FFPE). (a) Integrative analysis of FFPE-1 and FFPE-2 DBiT-seq data with scRNA-seq data from mouse embryos ranging from E9.5-E13.5(Cao et al., 2019). The two samples conformed well in the scRNA-seq data. (b) UMAP of integrated data showing 26 distinct clusters. (c) UMAP clusters color coded for all cell types identified by scRNA-seq data combined with two FFPE sample spatial pixels. (d) Spatial expression of select clusters and corresponding cell types superposed on the tissue image. (e) List of all cell types identified in Figure 3c and spatial tissue pixels from two FFPE samples.

bioRxiv preprint doi: https://doi.org/10.1101/2020.10.13.338475; this version posted October 14, 2020. The copyright holder for this preprint (which was not certified by peer review) is the author/funder, who has granted bioRxiv a license to display the preprint in perpetuity. It is made available under aCC-BY 4.0 International license.

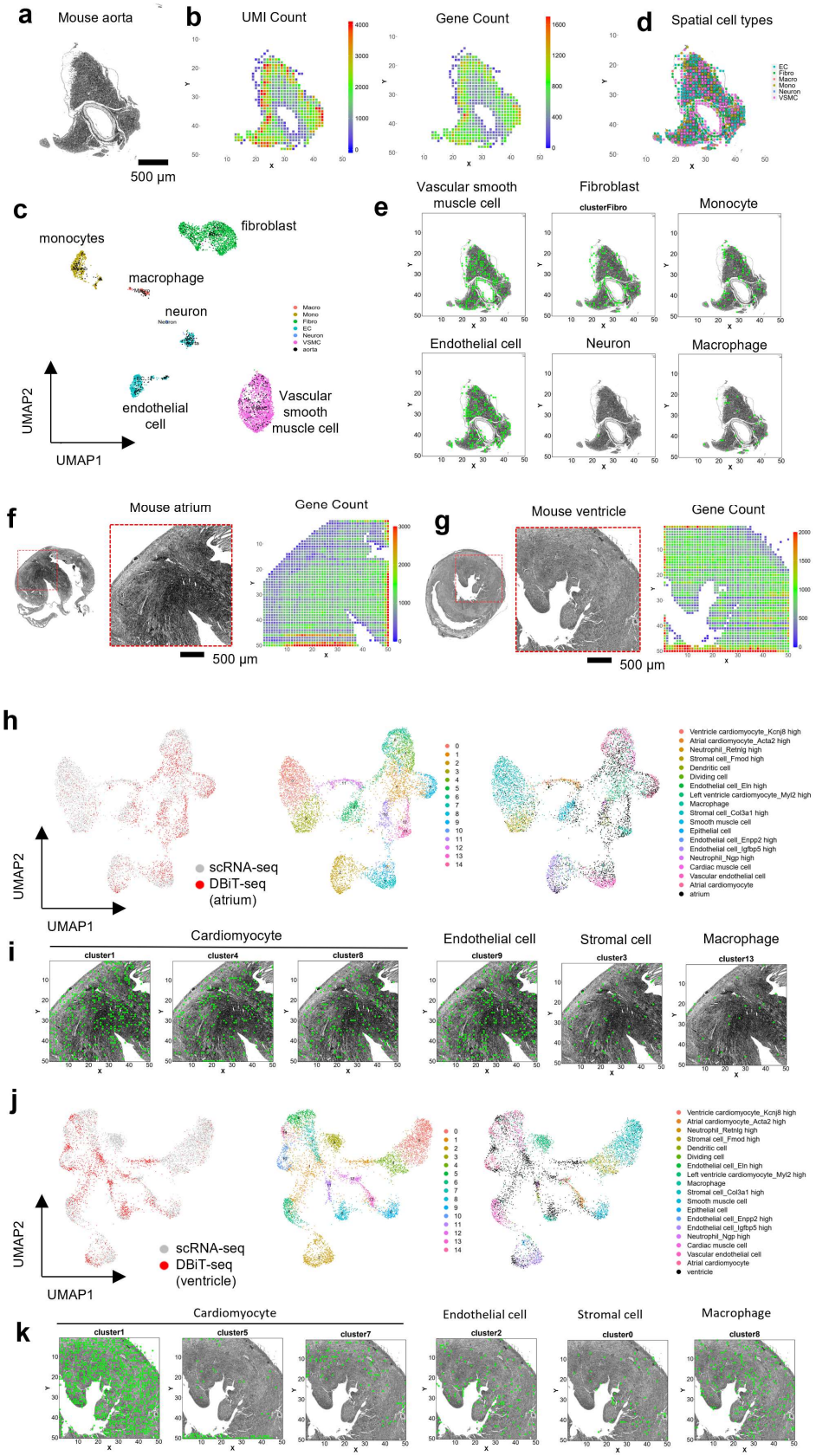

bioRxiv preprint doi: https://doi.org/10.1101/2020.10.13.338475; this version posted October 14, 2020. The copyright holder for this preprint (which was not certified by peer review) is the author/funder, who has granted bioRxiv a license to display the preprint in perpetuity. It is made available under aCC-BY 4.0 International license.

Figure 4. Spatial transcriptome mapping of adult mouse aorta, atrium and ventricle. (a) Bright field image of adult mouse aorta. Scale bar is 500 μm. (b) Spatial map of UMI and gene counts for each pixel. The average UMI count per pixel is ~1828 and gene count is ~664. (c) Clustering of spatial pixels with single-cell transcriptomes. The pixels conform to the clusters of scRNA-seq reference data. (d) Spatial distribution of major cell types annotated by integration with scRNA-seq data. These include endothelial cells (ECs), arterial fibroblasts (Fibro), macrophages (Macro), monocytes (Mono), Neurons and vascular smooth muscle cells (VSMCs). (e) Spatial distribution of individual cell types from Figure 4d. (f) Bright field image of a deparaffinized mouse atrium tissue section and the corresponding spatial gene count heatmap. (g) Bright field image of a deparaffinized mouse ventricle tissue section and the corresponding spatial gene count heatmap. (h) Clustering of the mouse atrium DBiT-seq data with scRNA-seq reference data. (i) Spatial distribution of representative annotated cells in atrium, see Figure S9 for the full panel. (j) Clustering of the mouse ventricle DBiT-seq data with scRNA-seq reference data. (k) Spatial distribution of representative annotated cells in ventricle, see Figure S9 for the full panel.

bioRxiv preprint doi: https://doi.org/10.1101/2020.10.13.338475; this version posted October 14, 2020. The copyright holder for this preprint (which was not certified by peer review) is the author/funder, who has granted bioRxiv a license to display the preprint in perpetuity. It is made available under aCC-BY 4.0 International license.

References

1. Krafft, A.E., Duncan, B.W., Bijwaard, K.E., Taubenberger, J.K. & Lichy, J.H. Optimization of the Isolation and Amplification of RNA From Formalin-fixed, Paraffin-embedded Tissue: The Armed Forces Institute of Pathology Experience and Literature Review. *Mol Diagn* **2**, 217-230 (1997).
2. Bass, B.P., Engel, K.B., Greytak, S.R. & Moore, H.M. A review of preanalytical factors affecting molecular, protein, and morphological analysis of formalin-fixed, paraffin-embedded (FFPE) tissue: how well do you know your FFPE specimen? *Arch Pathol Lab Med* **138**, 1520-1530 (2014).
3. Hedegaard, J., Thorsen, K., Lund, M.K., Hein, A.-M.K., Hamilton-Dutoit, S.J., Vang, S., Nordentoft, I., Birkenkamp-Demtröder, K., Kruhøffer, M., Hager, H., Knudsen, B., Andersen, C.L., Sørensen, K.D., Pedersen, J.S., Ørntoft, T.F. & Dyrskjøt, L. Next-Generation Sequencing of RNA and DNA Isolated from Paired Fresh-Frozen and Formalin-Fixed Paraffin-Embedded Samples of Human Cancer and Normal Tissue. *PLoS ONE* **9**, e98187 (2014).
4. Xie, R., Chung, J.-Y., Ylaya, K., Williams, R.L., Guerrero, N., Nakatsuka, N., Badie, C. & Hewitt, S.M. Factors Influencing the Degradation of Archival Formalin-Fixed Paraffin-Embedded Tissue Sections. *J. Histochem. Cytochem.* **59**, 356-365 (2011).
5. Graw, S., Meier, R., Minn, K., Bloomer, C., Godwin, A.K., Fridley, B., Vlad, A., Beyerlein, P. & Chien, J. Robust gene expression and mutation analyses of RNA-sequencing of formalin-fixed diagnostic tumor samples. *Sci Rep* **5**, 12335 (2015).
6. Sinicropi, D., Qu, K., Collin, F., Crager, M., Liu, M.-L., Pelham, R.J., Pho, M., Rossi, A.D., Jeong, J., Scott, A., Ambannavar, R., Zheng, C., Mena, R., Esteban, J., Stephans, J., Morlan, J. & Baker, J. Whole Transcriptome RNA-Seq Analysis of Breast Cancer Recurrence Risk Using Formalin-Fixed Paraffin-Embedded Tumor Tissue. *PLoS ONE* **7**, e40092 (2012).
7. Beck, A.H., Weng, Z., Witten, D.M., Zhu, S., Foley, J.W., Lacroute, P., Smith, C.L., Tibshirani, R., van de Rijn, M., Sidow, A. & West, R.B. 3′-End Sequencing for Expression Quantification (3SEQ) from Archival Tumor Samples. *PLoS ONE* **5**, e8768 (2010).
8. Klein, A.M., Mazutis, L., Akartuna, I., Tallapragada, N., Veres, A., Li, V., Peshkin, L., Weitz, D.A. & Kirschner, M.W. Droplet barcoding for single-cell transcriptomics applied to embryonic stem cells. *Cell* **161**, 1187-1201 (2015).

bioRxiv preprint doi: https://doi.org/10.1101/2020.10.13.338475; this version posted October 14, 2020. The copyright holder for this preprint (which was not certified by peer review) is the author/funder, who has granted bioRxiv a license to display the preprint in perpetuity. It is made available under aCC-BY 4.0 International license.

9. Macosko, E.Z., Basu, A., Satija, R., Nemesh, J., Shekhar, K., Goldman, M., Tirosh, I., Bialas, A.R., Kamitaki, N., Martersteck, E.M., Trombetta, J.J., Weitz, D.A., Sanes, J.R., Shalek, A.K., Regev, A. & McCarroll, S.A. Highly Parallel Genome-wide Expression Profiling of Individual Cells Using Nanoliter Droplets. *Cell* **161**, 1202-1214 (2015).
10. Kulkarni, A., Anderson, A.G., Merullo, D.P. & Konopka, G. Beyond bulk: a review of single cell transcriptomics methodologies and applications. *Curr Opin Biotechnol* **58**, 129-136 (2019).
11. Pichon, X., Lagha, M., Mueller, F. & Bertrand, E. A Growing Toolbox to Image Gene Expression in Single Cells: Sensitive Approaches for Demanding Challenges. *Mol Cell* **71**, 468-480 (2018).
12. Trcek, T., Lionnet, T., Shroff, H. & Lehmann, R. mRNA quantification using single-molecule FISH in Drosophila embryos. *Nat Protoc* **12**, 1326-1348 (2017).
13. Lubeck, E., Coskun, A.F., Zhiyentayev, T., Ahmad, M. & Cai, L. Single-cell in situ RNA profiling by sequential hybridization. *Nat Methods* **11**, 360-361 (2014).
14. Eng, C.L., Lawson, M., Zhu, Q., Dries, R., Koulena, N., Takei, Y., Yun, J., Cronin, C., Karp, C., Yuan, G.C. & Cai, L. Transcriptome-scale super-resolved imaging in tissues by RNA seqFISH. *Nature* **568**, 235-239 (2019).
15. Stahl, P.L., Salmen, F., Vickovic, S. et al. Visualization and analysis of gene expression in tissue sections by spatial transcriptomics. *Science* **353**, 78-82 (2016).
16. Rodriques, S.G., Stickels, R.R., Goeva, A., Martin, C.A., Murray, E., Vanderburg, C.R., Welch, J., Chen, L.M., Chen, F. & Macosko, E.Z. Slide-seq: A scalable technology for measuring genome-wide expression at high spatial resolution. *Science* **363**, 1463-1467 (2019).
17. Vickovic, S., Eraslan, G., Salmen, F., Klughammer, J., Stenbeck, L., Schapiro, D., Aijo, T., Bonneau, R., Bergenstrahle, L., Navarro, J.F., Gould, J., Griffin, G.K., Borg, A., Ronaghi, M., Frisen, J., Lundeberg, J., Regev, A. & Stahl, P.L. High-definition spatial transcriptomics for in situ tissue profiling. *Nat Methods* (2019).
18. Liu, Y., Yang, M., Deng, Y., Su, G., Guo, C.C., Zhang, D., Kim, D., Bai, Z., Xiao, Y. & Fan, R. High-Spatial-Resolution Multi-Omics Atlas Sequencing of Mouse Embryos via Deterministic Barcoding in Tissue. *bioRxiv*, 788992 (2019).
19. Svensson, V., Teichmann, S.A. & Stegle, O. SpatialDE: identification of spatially variable genes. *Nat. Meth.* **15**, 343-346 (2018).

bioRxiv preprint doi: https://doi.org/10.1101/2020.10.13.338475; this version posted October 14, 2020. The copyright holder for this preprint (which was not certified by peer review) is the author/funder, who has granted bioRxiv a license to display the preprint in perpetuity. It is made available under aCC-BY 4.0 International license.

20. Cao, J., Spielmann, M., Qiu, X., Huang, X., Ibrahim, D.M., Hill, A.J., Zhang, F., Mundlos, S., Christiansen, L., Steemers, F.J., Trapnell, C. & Shendure, J. The single-cell transcriptional landscape of mammalian organogenesis. *Nature* **566**, 496-502 (2019).
21. Hafemeister, C. & Satija, R. Normalization and variance stabilization of single-cell RNA-seq data using regularized negative binomial regression. *bioRxiv*, 576827 (2019).
22. Baron, M.H., Isern, J. & Fraser, S.T. The embryonic origins of erythropoiesis in mammals. *Blood* **119**, 4828-4837 (2012).
23. Kalluri, A.S., Vellarikkal, S.K., Edelman, E.R., Nguyen, L., Subramanian, A., Ellinor, P.T., Regev, A., Kathiresan, S. & Gupta, R.M. Single-Cell Analysis of the Normal Mouse Aorta Reveals Functionally Distinct Endothelial Cell Populations. *Circulation* **140**, 147-163 (2019).
24. Lynn Ray, J., Leach, R., Herbert, J.-M. & Benson, M. Isolation of vascular smooth muscle cells from a single murine aorta. *Methods in Cell Science* **23**, 185-188 (2001).
25. Zhou, P. & Pu, W.T. Recounting Cardiac Cellular Composition. *Circ. Res.* **118**, 368-370 (2016).
26. Schaum, N., Karkanias, J., Neff, N.F. et al. Single-cell transcriptomics of 20 mouse organs creates a Tabula Muris. *Nature* **562**, 367-372 (2018).
27. Navarro, J.F., Sjöstrand, J., Salmén, F., Lundeberg, J. & Ståhl, P.L. ST Pipeline: an automated pipeline for spatial mapping of unique transcripts. *Bioinformatics* **33**, 2591-2593 (2017).
28. Stuart, T., Butler, A., Hoffman, P., Hafemeister, C., Papalexi, E., Mauck III, W.M., Hao, Y., Stoeckius, M., Smibert, P. & Satija, R. Comprehensive integration of single-cell data. *Cell* **177**, 1888-1902. e1821 (2019).
29. Butler, A., Hoffman, P., Smibert, P., Papalexi, E. & Satija, R. Integrating single-cell transcriptomic data across different conditions, technologies, and species. *Nat. Biotechnol.* **36**, 411-420 (2018).
30. Aran, D., Looney, A.P., Liu, L., Wu, E., Fong, V., Hsu, A., Chak, S., Naikawadi, R.P., Wolters, P.J., Abate, A.R., Butte, A.J. & Bhattacharya, M. Reference-based analysis of lung single-cell sequencing reveals a transitional profibrotic macrophage. *Nat. Immunol.* **20**, 163-172 (2019).

bioRxiv preprint doi: https://doi.org/10.1101/2020.10.13.338475; this version posted October 14, 2020. The copyright holder for this preprint (which was not certified by peer review) is the author/funder, who has granted bioRxiv a license to display the preprint in perpetuity. It is made available under aCC-BY 4.0 International license.

SUPPLEMENTARY MATERIALS

Spatial transcriptome sequencing of FFPE tissues at the cellular level

Yang Liu[1,2], Archibald Enninful[1,2], Yanxiang Deng[1,2], and Rong Fan[1,2,3*]

[1] Department of Biomedical Engineering, Yale University, New Haven, CT 06520, USA

[2] Yale Stem Cell Center and Yale Cancer Center, Yale School of Medicine, New Haven, CT 06520, USA

[3]Human and Translational Immunology Program, Yale School of Medicine, New Haven, CT 06520, USA

* to whom all correspondence should be addressed. (R.F., rong.fan@yale.edu)

Supplementary Figures

Figure S1. Size distribution of cDNAs from FFPE and fresh frozen mouse embryo samples and correlation of sequencing data between FFPE sample and PFA-fixed frozen samples.

Figure S2. Differential Expressed Gene (DEG) heatmap of FFPE-1 and FFPE-2 (combined).

Figure S3. Clustering analysis of FFPE-1 and FFPE-2.

Figure S4. Spatial expression heatmap of select individual genes in FFPE-1 and FFPE-2.

Figure S5. SpatialDE patterns of FFPE-1 tissue section.

Figure S6. SpatialDE patterns of FFPE-2 tissue section. Spatial maps of 30 clusters were identified.

Figure S7. Clustering of the mouse aorta sample and visualization of individual genes.

Figure S8. *My6* gene distribution and UMAP of atrium and ventricle.

Figure S9. Spatial distribution of all 14 clusters in mouse atrium and ventricle.

Supplementary Tables

Table S1. DNA oligos used for PCR and preparation of sequencing library.

Table S2. DNA barcode sequences.

Table S3. Chemicals and reagents.

bioRxiv preprint doi: https://doi.org/10.1101/2020.10.13.338475; this version posted October 14, 2020. The copyright holder for this preprint (which was not certified by peer review) is the author/funder, who has granted bioRxiv a license to display the preprint in perpetuity. It is made available under aCC-BY 4.0 International license.

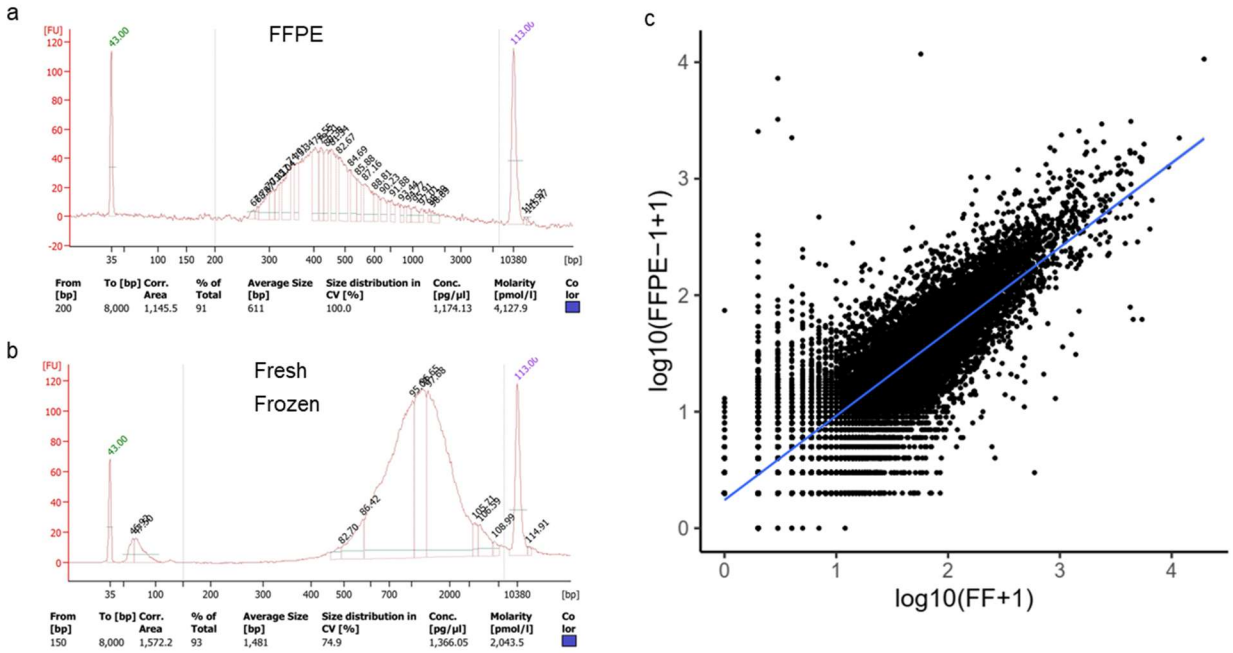

Figure S1. Size distribution of cDNAs from FFPE and fresh frozen mouse embryo samples and correlation of sequencing data between FFPE sample and PFA-fixed frozen samples. (a) FFPE cDNA bioanalyzer data. (b) Fresh Frozen cDNA bioanalyzer data. (c) Correlation of sequencing data between FFPE and fresh frozen samples. Pearson correlation coefficient R = 0.88.

bioRxiv preprint doi: https://doi.org/10.1101/2020.10.13.338475; this version posted October 14, 2020. The copyright holder for this preprint (which was not certified by peer review) is the author/funder, who has granted bioRxiv a license to display the preprint in perpetuity. It is made available under aCC-BY 4.0 International license.

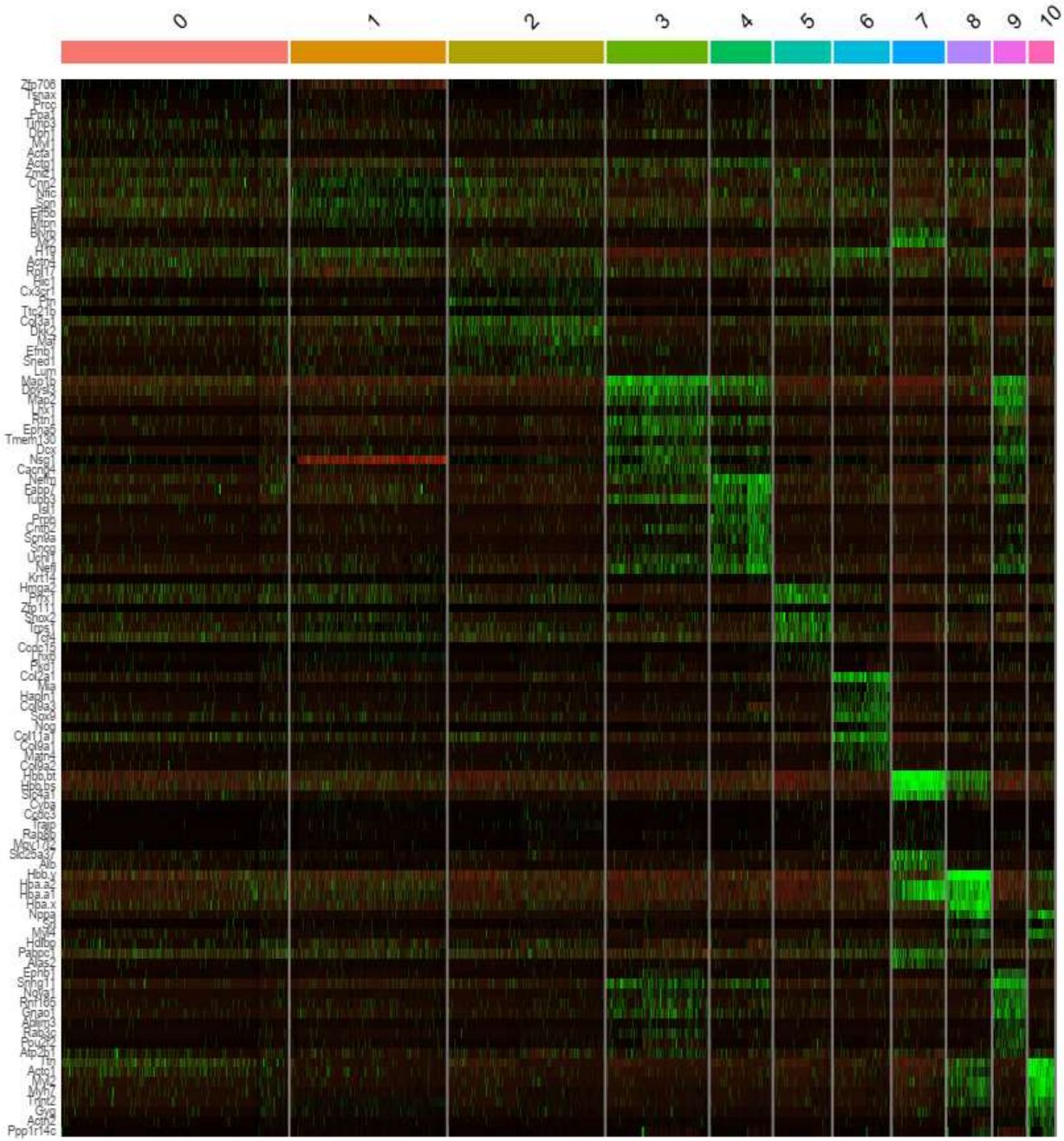

Figure S2. Differential Expressed Gene (DEG) heatmap of FFPE-1 and FFPE-2 (combined). This heatmap is a summary of top 10 DEGs in each cluster.

bioRxiv preprint doi: https://doi.org/10.1101/2020.10.13.338475; this version posted October 14, 2020. The copyright holder for this preprint (which was not certified by peer review) is the author/funder, who has granted bioRxiv a license to display the preprint in perpetuity. It is made available under aCC-BY 4.0 International license.

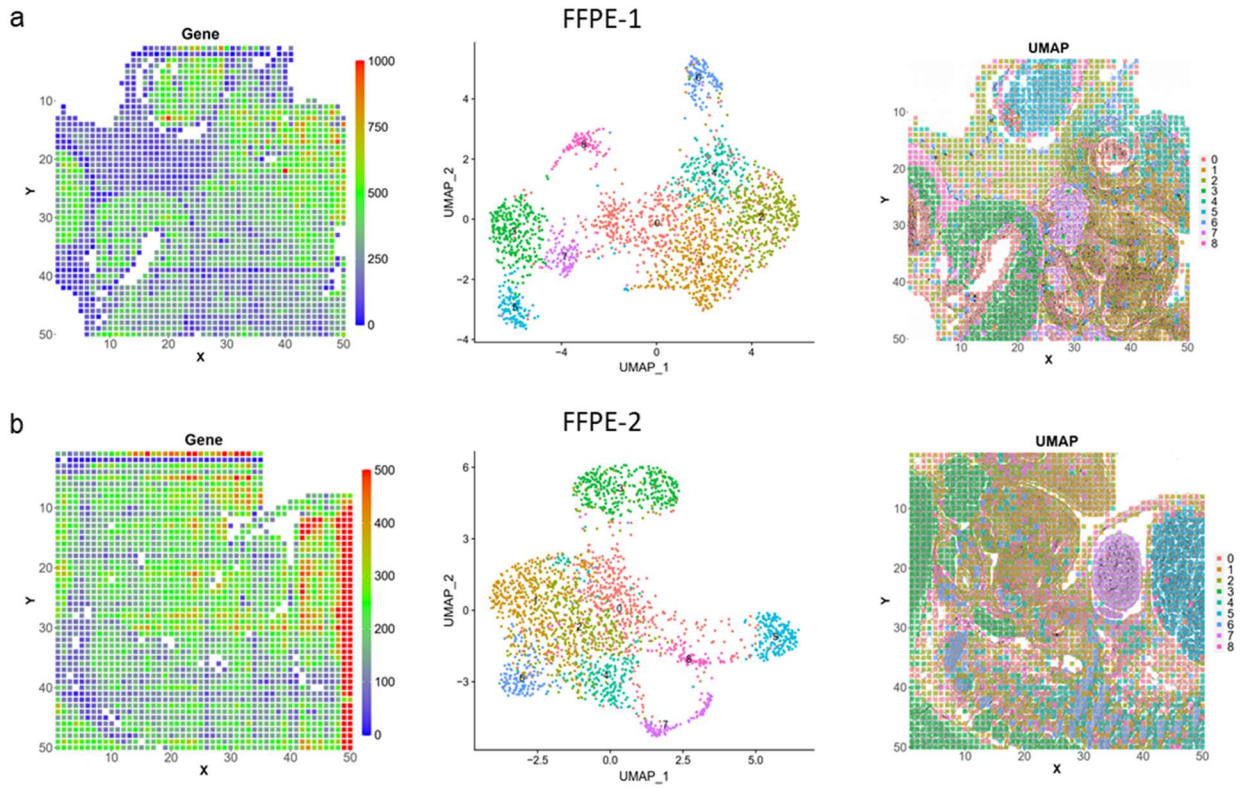

Figure S3. Clustering analysis of FFPE-1 and FFPE-2. (a) Clustering analysis of FFPE-1 only. Left: gene counts heat map; middle: UMAP of all FFPE-1 pixels; right: Spatial mapping of UMAP clusters. 8 clusters were observed. (b) Clustering analysis of FFPE-2. Left: gene counts heat map; middle: UMAP of all FFPE-1 pixels; right: Spatial mapping of UMAP clusters. 8 clusters were observed.

bioRxiv preprint doi: https://doi.org/10.1101/2020.10.13.338475; this version posted October 14, 2020. The copyright holder for this preprint (which was not certified by peer review) is the author/funder, who has granted bioRxiv a license to display the preprint in perpetuity. It is made available under aCC-BY 4.0 International license.

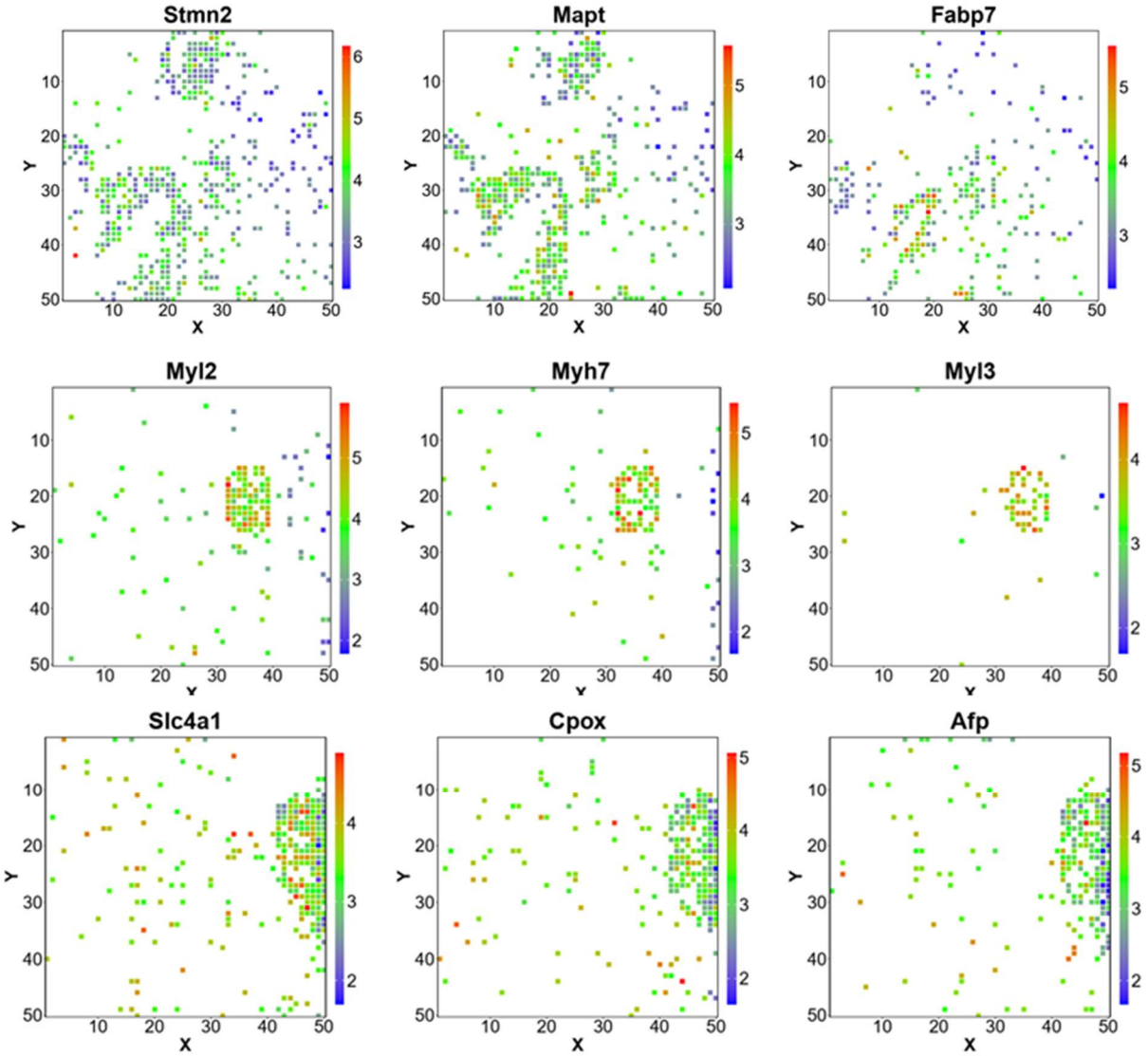

Figure S4. Spatial expression heatmap of select individual genes in FFPE-1 and FFPE-2.

bioRxiv preprint doi: https://doi.org/10.1101/2020.10.13.338475; this version posted October 14, 2020. The copyright holder for this preprint (which was not certified by peer review) is the author/funder, who has granted bioRxiv a license to display the preprint in perpetuity. It is made available under aCC-BY 4.0 International license.

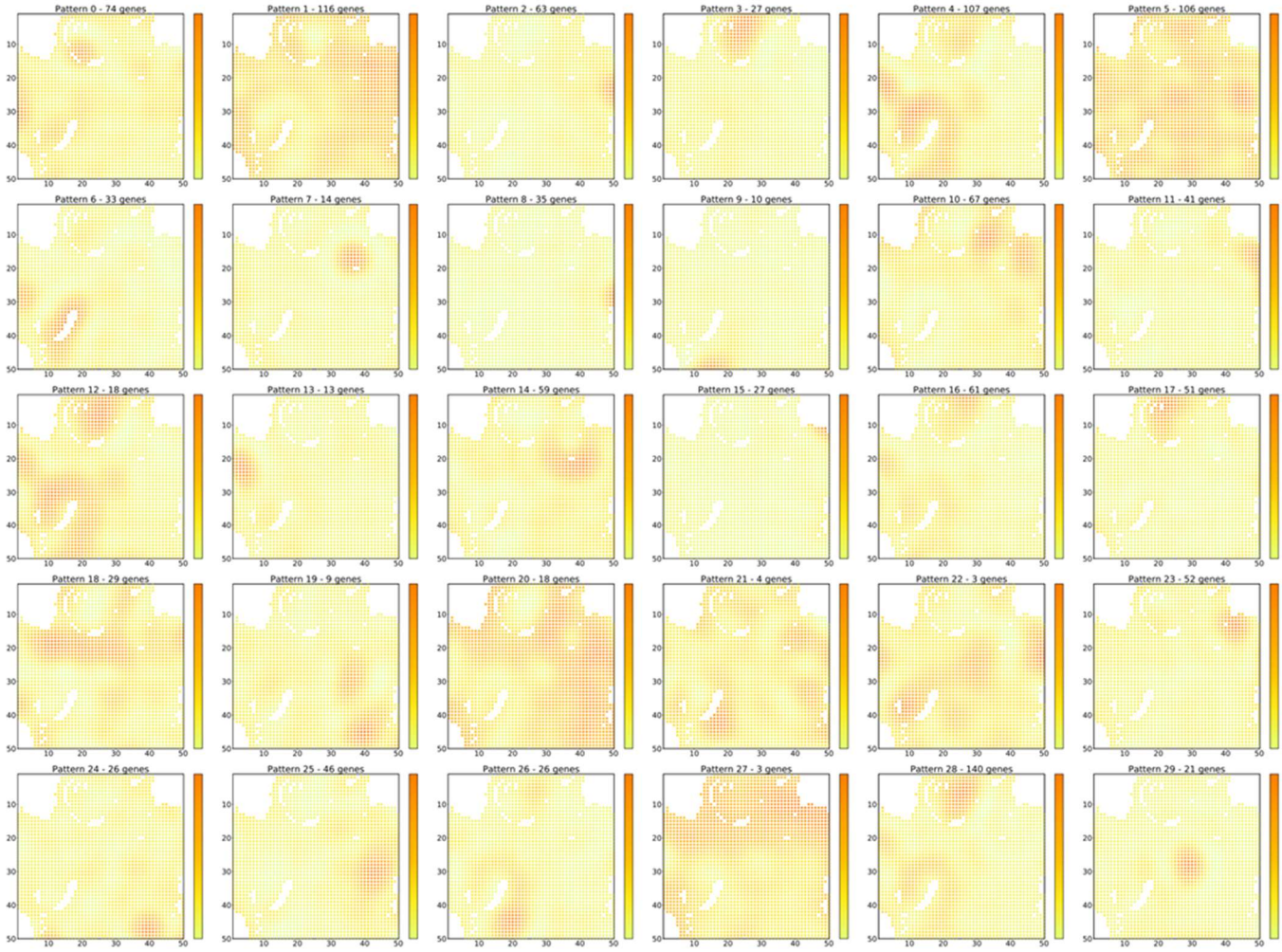

GO analysis for each pattern:

Pattern 0	neural precursor cell proliferation
Pattern 2	face morphogenesis, roof of mouth development
Pattern 3	forebrain neuron differentiation
Pattern 4	neuron development, forebrain development
Pattern 6	central nervous system development
Pattern 7	eye morphogenesis
Pattern 8	odontogenesis
Pattern 9	neurogenesis
Pattern 10	astrocyte differentiation, neurogenesis
Pattern 11	osteoblast differentiation
Pattern 12	axon extension
Pattern 13	spinal cord association neuron differentiation
Pattern 14	smooth muscle contraction, aorta morphogenesis
Pattern 15	epidermal cell division
Pattern 16	dendritic spine morphogenesis
Pattern 17	forebrain development
Pattern 18	skeletal system development
Pattern 19	muscle organ morphogenesis
Pattern 23	organ morphogenesis
Pattern 24	muscle organ development
Pattern 29	spinal cord motor neuron

Figure S5. SpatialDE patterns of FFPE-1 tissue section. Spatial maps of 30 clusters were identified. Select clusters with distinct GO pathways are listed.

bioRxiv preprint doi: https://doi.org/10.1101/2020.10.13.338475; this version posted October 14, 2020. The copyright holder for this preprint (which was not certified by peer review) is the author/funder, who has granted bioRxiv a license to display the preprint in perpetuity. It is made available under aCC-BY 4.0 International license.

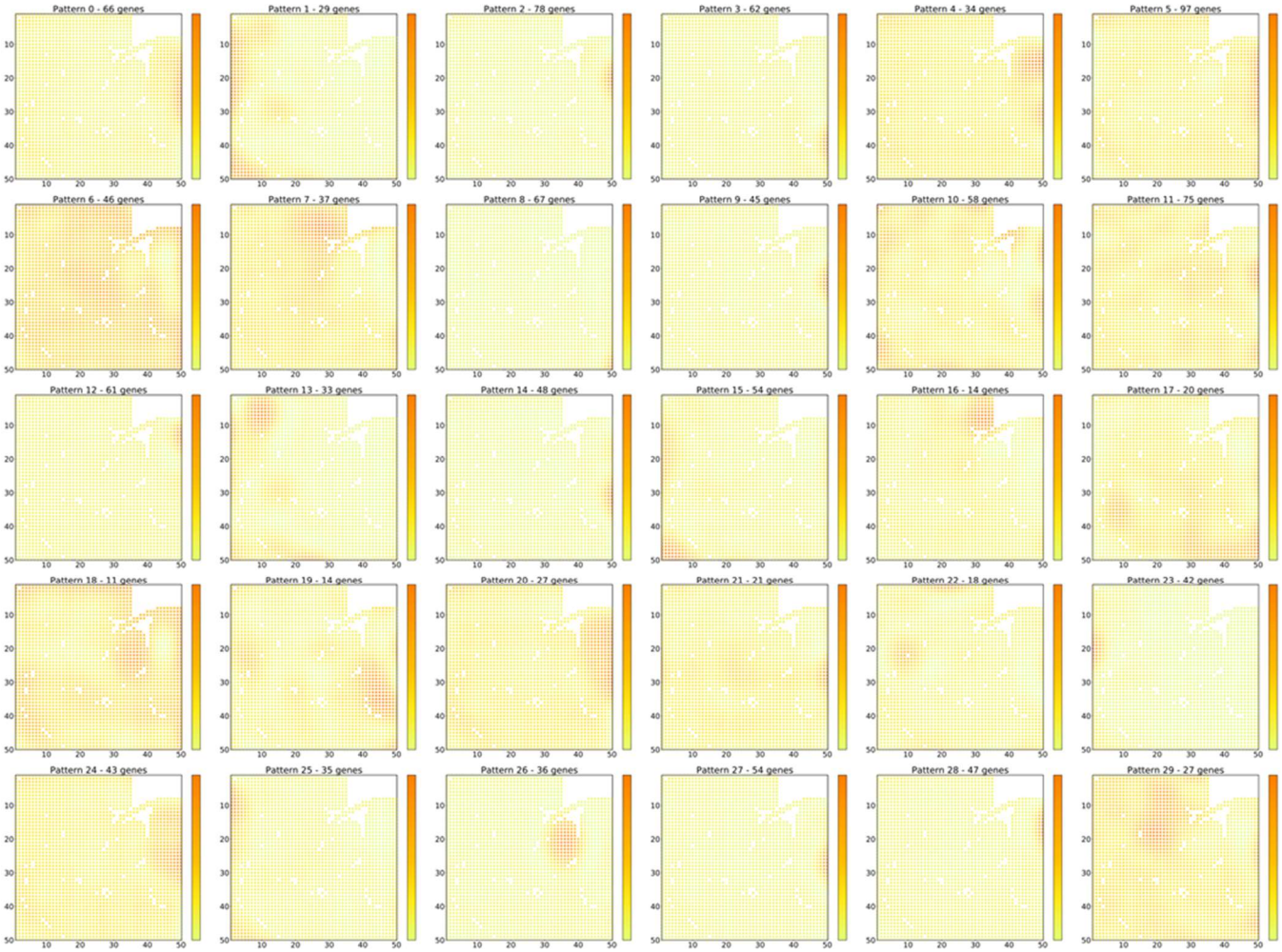

GO analysis for each pattern:

Pattern 0	myeloid cell development
Pattern 1	nervous system development
Pattern 2	cellular component organization
Pattern 5	peptide metabolic process
Pattern 6	anatomical structure morphogenesis
Pattern 7	roof of mouth development
Pattern 8	animal organ development
Pattern 12	cellular metabolic process
Pattern 13	nervous system development
Pattern 14	peptide metabolic process
Pattern 15	cell-cell signaling/synaptic signaling
Pattern 16	tube morphogenesis
Pattern 17	extracellular matrix organization
Pattern 20	heme metabolic process, protoporphyrinogen IX metabolic process
Pattern 23	neuron development
Pattern 25	neuron projection morphogenesis
Pattern 26	cardiac muscle contraction
Pattern 27	negative regulation of branching morphogenesis of a nerve
Pattern 29	epithelium development

Figure S6. SpatialDE patterns of FFPE-2 tissue section. Spatial maps of 30 clusters were identified. Select clusters with distinct GO pathways are listed.

bioRxiv preprint doi: https://doi.org/10.1101/2020.10.13.338475; this version posted October 14, 2020. The copyright holder for this preprint (which was not certified by peer review) is the author/funder, who has granted bioRxiv a license to display the preprint in perpetuity. It is made available under aCC-BY 4.0 International license.

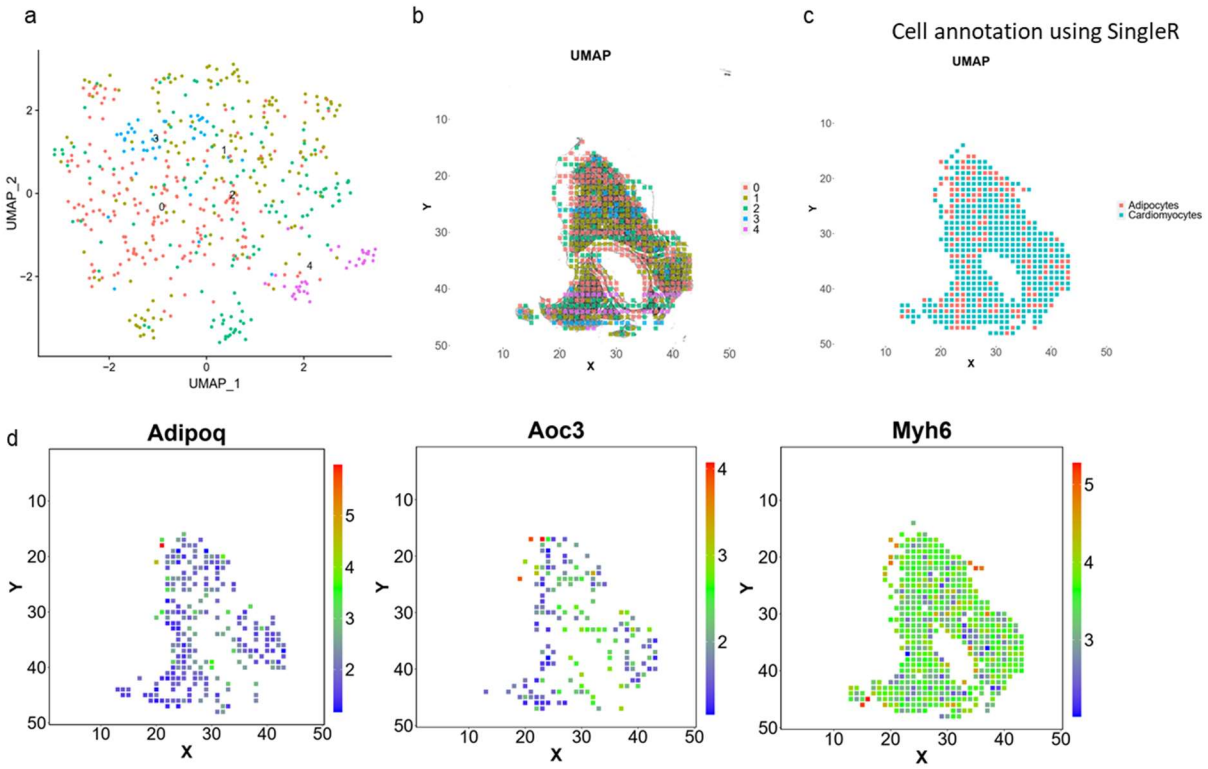

Figure S7. Clustering of the mouse aorta sample and visualization of individual genes. (a) UMAP clustering of all DBiT-seq pixels. (b) Spatial mapping of UMAP clusters in (a). (c) SingleR prediction of cell types using the built-in reference. (d) Spatial Mapping of individual genes: *Adipoq*, *Aoc3* and *Myh6*.

bioRxiv preprint doi: https://doi.org/10.1101/2020.10.13.338475; this version posted October 14, 2020. The copyright holder for this preprint (which was not certified by peer review) is the author/funder, who has granted bioRxiv a license to display the preprint in perpetuity. It is made available under aCC-BY 4.0 International license.

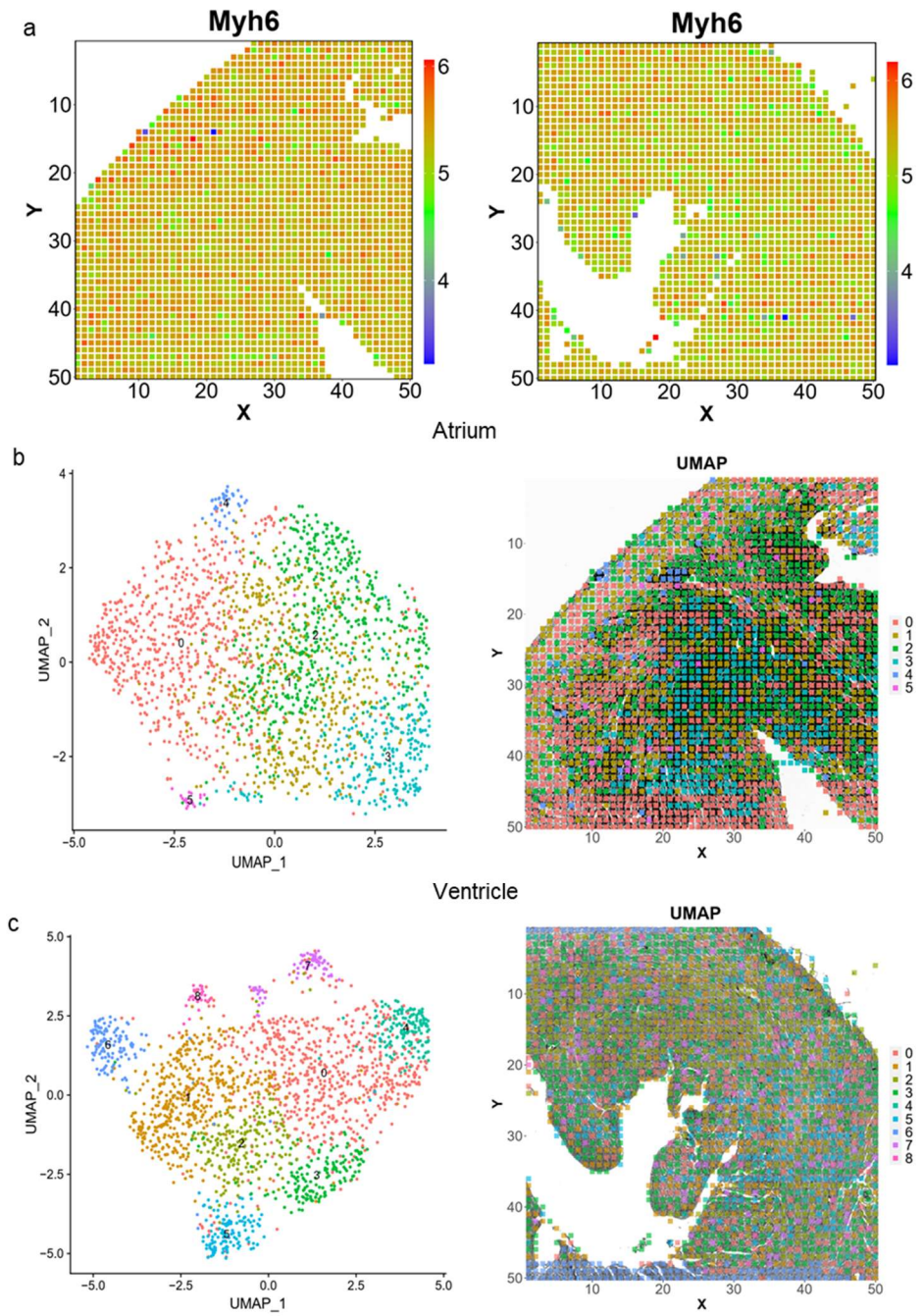

Figure S8. *My6* gene distribution and UMAP of atrium and ventricle. (a) *My6* gene in atrium (left) and ventricle (right). (b) Unsupervised clustering of atrium. (c) Unsupervised clustering of ventricle.

bioRxiv preprint doi: https://doi.org/10.1101/2020.10.13.338475; this version posted October 14, 2020. The copyright holder for this preprint (which was not certified by peer review) is the author/funder, who has granted bioRxiv a license to display the preprint in perpetuity. It is made available under aCC-BY 4.0 International license.

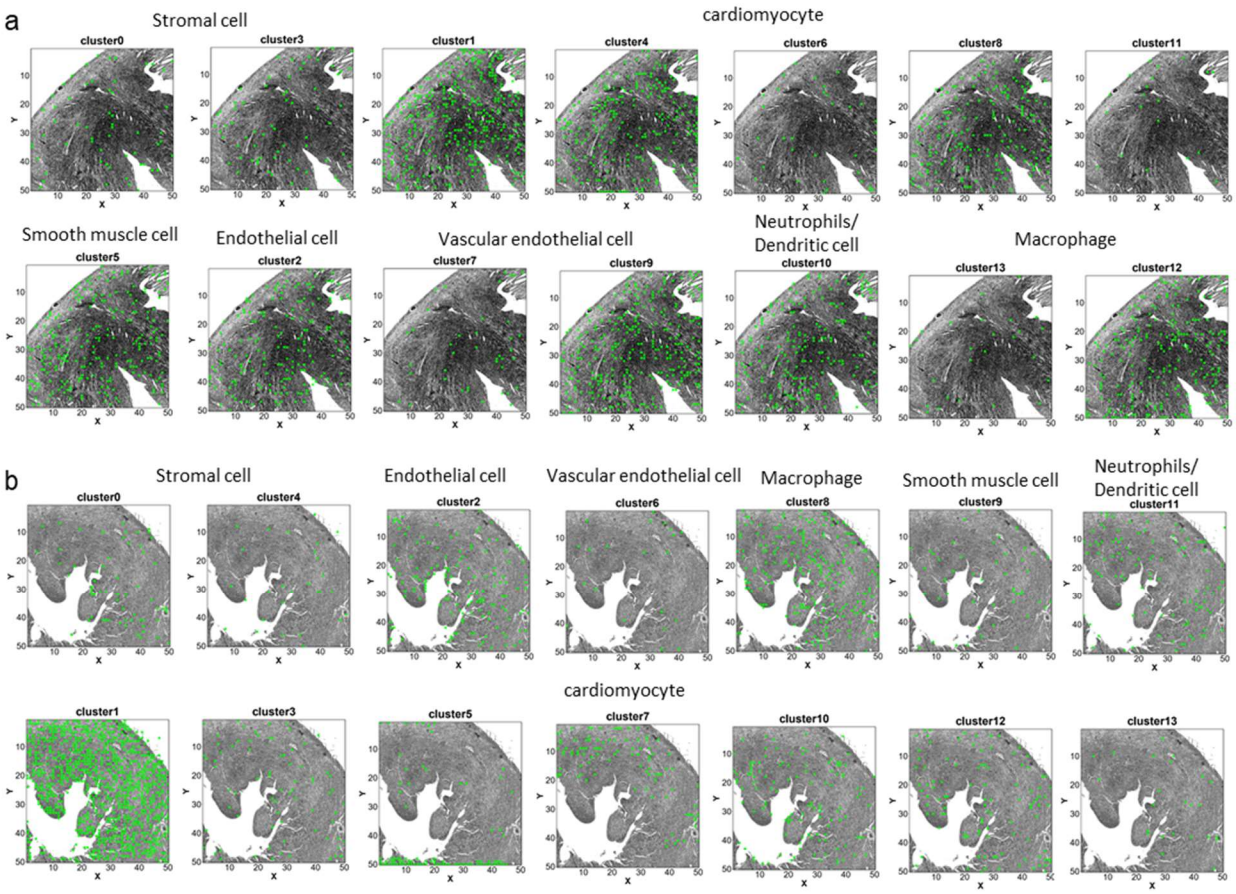

Figure S9. Spatial distribution of all 14 clusters in mouse atrium and ventricle. (a) cell distribution in mouse atrium. (b) cell distribution in mouse ventricle.

bioRxiv preprint doi: https://doi.org/10.1101/2020.10.13.338475; this version posted October 14, 2020. The copyright holder for this preprint (which was not certified by peer review) is the author/funder, who has granted bioRxiv a license to display the preprint in perpetuity. It is made available under aCC-BY 4.0 International license.

Table S1. DNA oligos used for PCR and preparation of sequencing library.

Oligo Name	Sequence
PCR Primer 1	CAAGCGTTGGCTTCTCGCATCT
PCR Primer 2	AAGCAGTGGTATCAACGCAGAGT
Ligation Linker	CGAATGCTCTGGCCTCTCAAGCACGTGGAT
Template Switch Oligo	AAGCAGTGGTATCAACGCAGAGTGAATrGrG+G
P5 oligo	AATGATACGGCGACCACCGAGATCTACACTAGATCGCTCGTCGGCAGCGTCAGATG TGTATAAGAGACAG
P7 oligo (701)	CAAGCAGAAGACGGCATACGAGATTCGCCTTAGTCTCGTGGGCTCGGAGATGTGTA TAAGAGACAGCAAGCGTTGGCTTCTCGCATCT
P7 oligo (702)	CAAGCAGAAGACGGCATACGAGATCTAGTACGGTCTCGTGGGCTCGGAGATGTGTA TAAGAGACAGCAAGCGTTGGCTTCTCGCATCT
P7 oligo (703)	CAAGCAGAAGACGGCATACGAGATTTCTGCCTGTCTCGTGGGCTCGGAGATGTGTA TAAGAGACAGCAAGCGTTGGCTTCTCGCATCT
P7 oligo (704)	CAAGCAGAAGACGGCATACGAGATGCTCAGGAGTCTCGTGGGCTCGGAGATGTGTA TAAGAGACAGCAAGCGTTGGCTTCTCGCATCT

Table S2. DNA barcode sequences.

1st Barcode	**Sequence**
Barcode A-1	/5Phos/AGGCCAGAGCATTCGAACGTGATTTTTTTTTTTTTTTTVN
Barcode A-2	/5Phos/AGGCCAGAGCATTCGAAACATCGTTTTTTTTTTTTTTTTVN
Barcode A-3	/5Phos/AGGCCAGAGCATTCGATGCCTAATTTTTTTTTTTTTTTTVN
Barcode A-4	/5Phos/AGGCCAGAGCATTCGAGTGGTCATTTTTTTTTTTTTTTTVN
Barcode A-5	/5Phos/AGGCCAGAGCATTCGACCACTGTTTTTTTTTTTTTTTTVN
Barcode A-6	/5Phos/AGGCCAGAGCATTCGACATTGGCTTTTTTTTTTTTTTTTVN
Barcode A-7	/5Phos/AGGCCAGAGCATTCGCAGATCTGTTTTTTTTTTTTTTTTVN
Barcode A-8	/5Phos/AGGCCAGAGCATTCGCATCAAGTTTTTTTTTTTTTTTTVN
Barcode A-9	/5Phos/AGGCCAGAGCATTCGCGCTGATCTTTTTTTTTTTTTTTTVN
Barcode A-10	/5Phos/AGGCCAGAGCATTCGACAAGCTATTTTTTTTTTTTTTTTVN
Barcode A-11	/5Phos/AGGCCAGAGCATTCGCTGTAGCCTTTTTTTTTTTTTTTTVN
Barcode A-12	/5Phos/AGGCCAGAGCATTCGAGTACAAGTTTTTTTTTTTTTTTTVN
Barcode A-13	/5Phos/AGGCCAGAGCATTCGAACAACCATTTTTTTTTTTTTTTTVN
Barcode A-14	/5Phos/AGGCCAGAGCATTCGAACCGAGATTTTTTTTTTTTTTTTVN
Barcode A-15	/5Phos/AGGCCAGAGCATTCGAACGCTTATTTTTTTTTTTTTTTVN
Barcode A-16	/5Phos/AGGCCAGAGCATTCGAAGACGGATTTTTTTTTTTTTTTTVN
Barcode A-17	/5Phos/AGGCCAGAGCATTCGAAGGTACATTTTTTTTTTTTTTTTVN
Barcode A-18	/5Phos/AGGCCAGAGCATTCGACACAGAATTTTTTTTTTTTTTTTVN
Barcode A-19	/5Phos/AGGCCAGAGCATTCGACAGCAGATTTTTTTTTTTTTTTTVN
Barcode A-20	/5Phos/AGGCCAGAGCATTCGACCTCCAATTTTTTTTTTTTTTTTVN

bioRxiv preprint doi: https://doi.org/10.1101/2020.10.13.338475; this version posted October 14, 2020. The copyright holder for this preprint (which was not certified by peer review) is the author/funder, who has granted bioRxiv a license to display the preprint in perpetuity. It is made available under aCC-BY 4.0 International license.

Barcode A-21	/5Phos/AGGCCAGAGCATTCGACGCTCGATTTTTTTTTTTTTTTVN
Barcode A-22	/5Phos/AGGCCAGAGCATTCGACGTATCATTTTTTTTTTTTTTTVN
Barcode A-23	/5Phos/AGGCCAGAGCATTCGACTATGCATTTTTTTTTTTTTTTVN
Barcode A-24	/5Phos/AGGCCAGAGCATTCGAGAGTCAATTTTTTTTTTTTTTTVN
Barcode A-25	/5Phos/AGGCCAGAGCATTCGAGATCGCATTTTTTTTTTTTTTTVN
Barcode A-26	/5Phos/AGGCCAGAGCATTCGAGCAGGAATTTTTTTTTTTTTTTVN
Barcode A-27	/5Phos/AGGCCAGAGCATTCGAGTCACTATTTTTTTTTTTTTTTVN
Barcode A-28	/5Phos/AGGCCAGAGCATTCGATCCTGTATTTTTTTTTTTTTTTVN
Barcode A-29	/5Phos/AGGCCAGAGCATTCGATTGAGGATTTTTTTTTTTTTTTVN
Barcode A-30	/5Phos/AGGCCAGAGCATTCGCAACCACATTTTTTTTTTTTTTTVN
Barcode A-31	/5Phos/AGGCCAGAGCATTCGGACTAGTATTTTTTTTTTTTTTTVN
Barcode A-32	/5Phos/AGGCCAGAGCATTCGCAATGGAATTTTTTTTTTTTTTTVN
Barcode A-33	/5Phos/AGGCCAGAGCATTCGCACTTCGATTTTTTTTTTTTTTTVN
Barcode A-34	/5Phos/AGGCCAGAGCATTCGCAGCGTTATTTTTTTTTTTTTTTVN
Barcode A-35	/5Phos/AGGCCAGAGCATTCGCATACCAATTTTTTTTTTTTTTTVN
Barcode A-36	/5Phos/AGGCCAGAGCATTCGCCAGTTCATTTTTTTTTTTTTTTVN
Barcode A-37	/5Phos/AGGCCAGAGCATTCGCCGAAGTATTTTTTTTTTTTTTTVN
Barcode A-38	/5Phos/AGGCCAGAGCATTCGCCGTGAGATTTTTTTTTTTTTTTVN
Barcode A-39	/5Phos/AGGCCAGAGCATTCGCCTCCTGATTTTTTTTTTTTTTTVN
Barcode A-40	/5Phos/AGGCCAGAGCATTCGCGAACTTATTTTTTTTTTTTTTTVN
Barcode A-41	/5Phos/AGGCCAGAGCATTCGCGACTGGATTTTTTTTTTTTTTTVN
Barcode A-42	/5Phos/AGGCCAGAGCATTCGCGCATACATTTTTTTTTTTTTTTVN
Barcode A-43	/5Phos/AGGCCAGAGCATTCGCTCAATGATTTTTTTTTTTTTTTVN
Barcode A-44	/5Phos/AGGCCAGAGCATTCGCTGAGCCATTTTTTTTTTTTTTTVN
Barcode A-45	/5Phos/AGGCCAGAGCATTCGCTGGCATATTTTTTTTTTTTTTTVN
Barcode A-46	/5Phos/AGGCCAGAGCATTCGGAATCTGATTTTTTTTTTTTTTTVN
Barcode A-47	/5Phos/AGGCCAGAGCATTCGCAAGACTATTTTTTTTTTTTTTTVN
Barcode A-48	/5Phos/AGGCCAGAGCATTCGGAGCTGAATTTTTTTTTTTTTTTVN
Barcode A-49	/5Phos/AGGCCAGAGCATTCGGATAGACATTTTTTTTTTTTTTTVN
Barcode A-50	/5Phos/AGGCCAGAGCATTCGGCCACATATTTTTTTTTTTTTTTVN
2nd Barcode	
Barcode B-1	/5Biosg/CAAGCGTTGGCTTCTCGCATCTNNNNNNNNNNAACGTGATATC CACGTGCTTGAG
Barcode B-2	/5Biosg/CAAGCGTTGGCTTCTCGCATCTNNNNNNNNNNAAACATCGATC CACGTGCTTGAG
Barcode B-3	/5Biosg/CAAGCGTTGGCTTCTCGCATCTNNNNNNNNNNATGCCTAAATC CACGTGCTTGAG
Barcode B-4	/5Biosg/CAAGCGTTGGCTTCTCGCATCTNNNNNNNNNNAGTGGTCAATC CACGTGCTTGAG
Barcode B-5	/5Biosg/CAAGCGTTGGCTTCTCGCATCTNNNNNNNNNNACCACTGTATC CACGTGCTTGAG
Barcode B-6	/5Biosg/CAAGCGTTGGCTTCTCGCATCTNNNNNNNNNNACATTGGCATC CACGTGCTTGAG
Barcode B-7	/5Biosg/CAAGCGTTGGCTTCTCGCATCTNNNNNNNNNNCAGATCTGATC CACGTGCTTGAG

bioRxiv preprint doi: https://doi.org/10.1101/2020.10.13.338475; this version posted October 14, 2020. The copyright holder for this preprint (which was not certified by peer review) is the author/funder, who has granted bioRxiv a license to display the preprint in perpetuity. It is made available under aCC-BY 4.0 International license.

Barcode B-8	/5Biosg/CAAGCGTTGGCTTCTCGCATCTNNNNNNNNNNCATCAAGTATC CACGTGCTTGAG
Barcode B-9	/5Biosg/CAAGCGTTGGCTTCTCGCATCTNNNNNNNNNNCGCTGATCATC CACGTGCTTGAG
Barcode B-10	/5Biosg/CAAGCGTTGGCTTCTCGCATCTNNNNNNNNNNACAAGCTAATC CACGTGCTTGAG
Barcode B-11	/5Biosg/CAAGCGTTGGCTTCTCGCATCTNNNNNNNNNNCTGTAGCCATC CACGTGCTTGAG
Barcode B-12	/5Biosg/CAAGCGTTGGCTTCTCGCATCTNNNNNNNNNNAGTACAAGATC CACGTGCTTGAG
Barcode B-13	/5Biosg/CAAGCGTTGGCTTCTCGCATCTNNNNNNNNNNAACAACCAATC CACGTGCTTGAG
Barcode B-14	/5Biosg/CAAGCGTTGGCTTCTCGCATCTNNNNNNNNNNAACCGAGAATC CACGTGCTTGAG
Barcode B-15	/5Biosg/CAAGCGTTGGCTTCTCGCATCTNNNNNNNNNNAACGCTTAATC CACGTGCTTGAG
Barcode B-16	/5Biosg/CAAGCGTTGGCTTCTCGCATCTNNNNNNNNNNAAGACGGAATC CACGTGCTTGAG
Barcode B-17	/5Biosg/CAAGCGTTGGCTTCTCGCATCTNNNNNNNNNNAAGGTACAATC CACGTGCTTGAG
Barcode B-18	/5Biosg/CAAGCGTTGGCTTCTCGCATCTNNNNNNNNNNACACAGAAATC CACGTGCTTGAG
Barcode B-19	/5Biosg/CAAGCGTTGGCTTCTCGCATCTNNNNNNNNNNACAGCAGAATC CACGTGCTTGAG
Barcode B-20	/5Biosg/CAAGCGTTGGCTTCTCGCATCTNNNNNNNNNNACCTCCAAATC CACGTGCTTGAG
Barcode B-21	/5Biosg/CAAGCGTTGGCTTCTCGCATCTNNNNNNNNNNACGCTCGAATC CACGTGCTTGAG
Barcode B-22	/5Biosg/CAAGCGTTGGCTTCTCGCATCTNNNNNNNNNNACGTATCAATC CACGTGCTTGAG
Barcode B-23	/5Biosg/CAAGCGTTGGCTTCTCGCATCTNNNNNNNNNNACTATGCAATC CACGTGCTTGAG
Barcode B-24	/5Biosg/CAAGCGTTGGCTTCTCGCATCTNNNNNNNNNNAGAGTCAAATC CACGTGCTTGAG
Barcode B-25	/5Biosg/CAAGCGTTGGCTTCTCGCATCTNNNNNNNNNNAGATCGCAATC CACGTGCTTGAG
Barcode B-26	/5Biosg/CAAGCGTTGGCTTCTCGCATCTNNNNNNNNNNAGCAGGAAATC CACGTGCTTGAG
Barcode B-27	/5Biosg/CAAGCGTTGGCTTCTCGCATCTNNNNNNNNNNAGTCACTAATC CACGTGCTTGAG
Barcode B-28	/5Biosg/CAAGCGTTGGCTTCTCGCATCTNNNNNNNNNNATCCTGTAATCC ACGTGCTTGAG
Barcode B-29	/5Biosg/CAAGCGTTGGCTTCTCGCATCTNNNNNNNNNNATTGAGGAATC CACGTGCTTGAG
Barcode B-30	/5Biosg/CAAGCGTTGGCTTCTCGCATCTNNNNNNNNNNCAACCACAATC CACGTGCTTGAG
Barcode B-31	/5Biosg/CAAGCGTTGGCTTCTCGCATCTNNNNNNNNNNGACTAGTAATC CACGTGCTTGAG
Barcode B-32	/5Biosg/CAAGCGTTGGCTTCTCGCATCTNNNNNNNNNNCAATGGAAATC CACGTGCTTGAG
Barcode B-33	/5Biosg/CAAGCGTTGGCTTCTCGCATCTNNNNNNNNNNCACTTCGAATC CACGTGCTTGAG
Barcode B-34	/5Biosg/CAAGCGTTGGCTTCTCGCATCTNNNNNNNNNNCAGCGTTAATC CACGTGCTTGAG

bioRxiv preprint doi: https://doi.org/10.1101/2020.10.13.338475; this version posted October 14, 2020. The copyright holder for this preprint (which was not certified by peer review) is the author/funder, who has granted bioRxiv a license to display the preprint in perpetuity. It is made available under aCC-BY 4.0 International license.

Barcode B-35	/5Biosg/CAAGCGTTGGCTTCTCGCATCTNNNNNNNNNNCATACCAAATC CACGTGCTTGAG
Barcode B-36	/5Biosg/CAAGCGTTGGCTTCTCGCATCTNNNNNNNNNNCCAGTTCAATC CACGTGCTTGAG
Barcode B-37	/5Biosg/CAAGCGTTGGCTTCTCGCATCTNNNNNNNNNNCCGAAGTAATC CACGTGCTTGAG
Barcode B-38	/5Biosg/CAAGCGTTGGCTTCTCGCATCTNNNNNNNNNNCCGTGAGAATC CACGTGCTTGAG
Barcode B-39	/5Biosg/CAAGCGTTGGCTTCTCGCATCTNNNNNNNNNNCCTCCTGAATC CACGTGCTTGAG
Barcode B-40	/5Biosg/CAAGCGTTGGCTTCTCGCATCTNNNNNNNNNNCGAACTTAATC CACGTGCTTGAG
Barcode B-41	/5Biosg/CAAGCGTTGGCTTCTCGCATCTNNNNNNNNNNCGACTGGAATC CACGTGCTTGAG
Barcode B-42	/5Biosg/CAAGCGTTGGCTTCTCGCATCTNNNNNNNNNNCGCATACAATC CACGTGCTTGAG
Barcode B-43	/5Biosg/CAAGCGTTGGCTTCTCGCATCTNNNNNNNNNNCTCAATGAATC CACGTGCTTGAG
Barcode B-44	/5Biosg/CAAGCGTTGGCTTCTCGCATCTNNNNNNNNNNCTGAGCCAATC CACGTGCTTGAG
Barcode B-45	/5Biosg/CAAGCGTTGGCTTCTCGCATCTNNNNNNNNNNCTGGCATAATC CACGTGCTTGAG
Barcode B-46	/5Biosg/CAAGCGTTGGCTTCTCGCATCTNNNNNNNNNNGAATCTGAATC CACGTGCTTGAG
Barcode B-47	/5Biosg/CAAGCGTTGGCTTCTCGCATCTNNNNNNNNNNCAAGACTAATC CACGTGCTTGAG
Barcode B-48	/5Biosg/CAAGCGTTGGCTTCTCGCATCTNNNNNNNNNNGAGCTGAAATC CACGTGCTTGAG
Barcode B-49	/5Biosg/CAAGCGTTGGCTTCTCGCATCTNNNNNNNNNNGATAGACAATC CACGTGCTTGAG
Barcode B-50	/5Biosg/CAAGCGTTGGCTTCTCGCATCTNNNNNNNNNNGCCACATAATC CACGTGCTTGAG

Table S3. Chemicals and reagents.

Reagent List		
Name	Cat. Number	Vender
Maxima H Minus	EP7051	Thermo Fisher
dNTP mix	R0192	Thermo Fisher
RNase Inhibitor	Y9240L	Enzymatics
SUPERase• In™ RNase Inhibitor	AM2694	Thermo Fisher
T4 DNA Ligase	M0202L	New England Biolabs
Ampure XP beads	A63880	Beckman Coulter
Dynabeads MyOne C1	65001	Thermo Fisher
	65002	
Nextera XT DNA Preparation Kit	FC-131-1024	Illumina

bioRxiv preprint doi: https://doi.org/10.1101/2020.10.13.338475; this version posted October 14, 2020. The copyright holder for this preprint (which was not certified by peer review) is the author/funder, who has granted bioRxiv a license to display the preprint in perpetuity. It is made available under aCC-BY 4.0 International license.

Kapa Hotstart HiFi ReadyMix	KK2601	Kapa Biosystems
Proteinase K, recombinant, PCR grade	EO0491	Thermo Fisher
Buffer and chemical supplies		
RNAse free water	10977015	Invitrogen
Xylene	534056-4L	Sigma
Ethanol	187380-4L	Sigma
Formaldehyde solution	F8775-25ML	Sigma
Triton X-100	T8787-100ML	Sigma
NEBuffer 3.1	B7203S	New England Biolabs
T4 DNA Ligase Reaction Buffer	B0202S	New England Biolabs
Binding and washing (B&W) Buffer (2x)	15568025	Thermo Fisher
	AM9261	Thermo Fisher
	AM9760G	Thermo Fisher
PMSF	10837091001	Sigma
Tween 20	3005	Thermo Fisher